TECHNICAL REPORT
https://doi.org/10.1038/s41594-021-00575-9

nature structural & molecular biology

A chemical genetics approach to examine the functions of AAA proteins

Tommaso Cupido[1,3], Natalie H. Jones[1,2,3], Michael J. Grasso[1], Rudolf Pisa[1,2] and Tarun M. Kapoor[1]✉

The structural conservation across the AAA (ATPases associated with diverse cellular activities) protein family makes designing selective chemical inhibitors challenging. Here, we identify a triazolopyridine-based fragment that binds the AAA domain of human katanin, a microtubule-severing protein. We have developed a model for compound binding and designed ASPIR-1 (allele-specific, proximity-induced reactivity-based inhibitor-1), a cell-permeable compound that selectively inhibits katanin with an engineered cysteine mutation. Only in cells expressing mutant katanin does ASPIR-1 treatment increase the accumulation of CAMSAP2 at microtubule minus ends, confirming specific on-target cellular activity. Importantly, ASPIR-1 also selectively inhibits engineered cysteine mutants of human VPS4B and FIGL1—AAA proteins, involved in organelle dynamics and genome stability, respectively. Structural studies confirm our model for compound binding at the AAA ATPase site and the proximity-induced reactivity-based inhibition. Together, our findings suggest a chemical genetics approach to decipher AAA protein functions across essential cellular processes and to test hypotheses for developing therapeutics.

ATPases associated with diverse cellular activities (AAAs) are molecular motors that typically function as hexameric assemblies to remodel or translocate proteins or nucleic acid substrates[1,2]. Despite extensive structural and biochemical characterization, examining the functions of AAA proteins in cells remains challenging[3,4]. AAA proteins have key roles in dynamic cellular processes, including DNA replication and repair, microtubule cytoskeleton dynamics and intracellular vesicle trafficking[5–7]. Furthermore, dysregulation of AAA protein activity has been linked to human disease, and these enzymes have emerged as potential targets for pharmacological modulation, especially in cancer[8,9]. Therefore, chemical probes that allow acute inhibition of individual AAA proteins with high selectivity would be powerful tools to dissect their cellular functions. In addition, these probes can be used to decipher the changes in the activities of these proteins that cause disease. Currently, we lack such chemical tools for most of the approximately 100 human AAA proteins.

Designing allele-specific chemical inhibitors (also called the 'bump-hole' approach) is an effective chemical genetics strategy that has been used to dissect the functions of selected proteins within large superfamilies such as kinases and bromo and extra-terminal (BET) proteins[10,11]. This approach relies on two steps. First, a functionally silent mutation is introduced into a compound-binding site of a selected protein target to generate a variant allele that does not exist naturally. Second, the compound is modified to increase its affinity for the engineered binding site, while reducing its ability to interact with the unmodified binding site in related native proteins. In many cases, mutant protein-modified inhibitor pairs can be readily generated for multiple proteins within a superfamily to selectively probe their functions. However, a chemical genetics approach that could be used to systematically examine AAA protein function has not been developed.

AAA proteins are defined by the AAA domain, an α/β-Rossmann fold-like domain that plays a central role in their mechanochemical cycle[1,2]. The AAA domain binds adenosine-5′-triphosphate (ATP)[1,3], and can also mediate interactions with protein or nucleic acid substrates. Within this domain, the ATP-binding site is composed of residues located in six motifs: the N-loop, P-loop (or Walker A), hinge, helix-7, sensor-II and Walker B motifs within a single AAA domain[4]. ATP hydrolysis depends on an Arg-finger motif, which is provided by an adjacent AAA domain within a higher-order (typically hexameric) assembly[4]. Developing allele-specific inhibitors for AAA proteins would involve identifying a compound that binds the ATP-binding site, which is conserved across AAA proteins. In addition, understanding how this compound binds the AAA domain is needed to guide chemical modifications and the introduction of functionally silent point mutations in the nucleotide-binding site to achieve potent and selective inhibition of a single AAA protein.

ATP-competitive inhibitors that target the AAA proteins spastin and VCP/p97 have been developed[12,13]. In the case of spastin, an approach termed resistance analysis during design (RADD) was employed to design spastazoline, a pyrazolopyrimidine-based compound, as well as diaminotriazole-based compounds[14]. RADD involves testing selected inhibitor scaffolds against engineered, biochemically active mutant alleles of a target protein. Mutations that alter compound potency identify residues in the target protein that are probably involved in inhibitor interactions and help establish robust models for inhibitor–target binding[15]. By contrast, the VCP/p97 inhibitor CB-5083, a 4-benzylamino-pyranopyrimidine-based compound that entered clinical trials, was developed by extensive follow-up optimization of a 'hit' from large-scale screening of chemical libraries[12,16]. Structural studies have shown that both spastazoline and CB-5083 bind at the ATP-binding site[17,18]. However, the available data do not readily suggest a chemical scaffold that can target multiple AAA proteins, as is needed to develop the allele-specific inhibitor approach.

In this Article, we report an allele-specific covalent inhibitor for AAA proteins, which we named ASPIR-1 (allele-specific, proximity-induced reactivity-based inhibitor-1). Employing RADD, we characterized how a low-affinity triazolopyridine-based

[1]Laboratory of Chemistry and Cell Biology, The Rockefeller University, New York, NY, USA. [2]Tri-Institutional PhD Program in Chemical Biology, The Rockefeller University, New York, NY, USA. [3]These authors contributed equally: Tommaso Cupido, Natalie H. Jones. ✉e-mail: kapoor@rockefeller.edu

fragment binds to the ATP-binding site of katanin, an AAA protein that regulates microtubule organization. The RADD model guided modification of this inhibitor scaffold with a reactive functional group that can undergo a proximity-induced reaction with a cysteine residue, which can be introduced as a biochemically silent mutation in the AAA ATPase site. Our studies show that ASPIR-1 treatment phenocopies RNA interference (RNAi)-mediated katanin knockdown specifically in cells that express the cysteine-mutant allele of katanin. We also show that an equivalent cysteine mutation can be used to engineer ASPIR-1 sensitivity in two additional AAA proteins (vacuolar protein sorting-associated protein B (VPS4B) and fidgetin-like 1 (FIGL1)), and we support the RADD binding model and covalent inhibition with structural data.

Results

RADD analysis of triazolopyridine compounds binding katanin. To develop an allele-specific inhibitor strategy for the AAA protein family we focused on katanin-p60 (hereafter, katanin), a microtubule-severing enzyme required for the assembly and maintenance of specialized microtubule-based structures such as those found in dividing cells, cilia and neurons[6]. Katanin belongs to the largest clade of the AAA family, which also includes VCP/p97, spastin, FIGL1 and VPS4, among others[2].

To apply the RADD approach to katanin, we analyzed its ATP-binding site and identified 'variability hotspot residues'. These residues in the ATP-binding site are relatively less conserved and, when replaced by residues found at equivalent sites in other AAA proteins, are predicted to yield alleles that retain biochemical activity[13] (Fig. 1a,b). We generated a recombinant construct containing the human katanin AAA domain (aa 171–491, hereafter kata-AAA-WT; Fig. 1b,c) (protein purification described in Methods and Supplementary Note 1). This construct is based on a construct we used previously for spastin, a related microtubule-severing AAA protein[17]. We then compared binding of adenosine 5′-diphosphate (ADP) to kata-AAA-WT and seven engineered variability hotspot mutant constructs (L214C, L214V, T253N, T253C, A419L, T422A and T422K), with specific mutations selected based on structure-guided sequence analyses (Supplementary Table 1), using differential scanning fluorimetry (DSF)[19]. In this assay, the melting temperature of kata-AAA-WT increased by ~5 °C (ΔT_m) in the presence of ADP (1 mM, Fig. 1d,e and Supplementary Table 2). Five alleles with mutations at the variability hotspots revealed shifts in melting temperatures similar to that of the wild-type (WT) protein (ΔT_m, +4 °C to +6 °C; Fig. 1e and Supplementary Table 2). However, the L214V mutation decreased the melting temperature and reduced ADP-binding-dependent stabilization of this construct, and the T253C mutation substantially increased the melting temperature of the construct (Fig. 1e and Supplementary Table 2). Therefore, for further analyses, we selected L214C, T253N, A419L and T422K alleles, providing one mutant allele for each variability hotspot residue.

To identify chemical starting points that could be used for designing allele-specific katanin inhibitors, we focused on a triazolopyridine scaffold, which is based on a pharmacophore we hypothesized to be common to inhibitors that target AAA ATP-binding sites[13]. In particular, we selected compound **1** (8-phenyl-triazolopyridine-2-amine, Fig. 2a; synthesis described in Supplementary Note 2), as a low-molecular-weight compound that stabilizes kata-AAA-WT against thermal denaturation ($\Delta T_m \approx +4$ °C at 500 µM, Fig. 2b and Extended Data Fig. 1a,b). DSF analyses reveal that three of the four variability hotspot mutations reduced compound binding, while one mutation (A419L) increased compound binding (Fig. 2b). Only three of the four binding poses obtained from computational docking of compound **1** onto the katanin ATP-binding site are plausible, as they account for the changes in compound binding observed for the variability hotspot alleles (poses 1–3, Extended Data Fig. 1c).

To distinguish between these compound binding poses we generated three analogs with substitutions on the C8 or C2 positions of the triazolopyridine (compounds **2**–**4**, Fig. 2a; syntheses are described in Supplementary Note 2). Isothermal titration calorimetry (ITC) and DSF analyses revealed that although the affinities of these fragment compounds for kata-AAA-WT remain low (micromolar), the analogs with the C8 substitutions bind kata-AAA-WT with higher affinity than compound **1** (Fig. 2a,c and Extended Data Fig. 1d,e). The binding affinity for kata-AAA-WT is reduced in the case of the analog with a C2 substitution (Fig. 2a,c). Applying our RADD approach to these compound **1** analogs suggests a model in which the triazolopyridine scaffold binds the ATP-binding site of katanin with the C8 substituent pointing toward the T422 and A419 variability hotspot residues, and the C2 substituent oriented towards the solvent (Fig. 2a,d,e).

Allele-specific inhibition of a cysteine-mutant katanin. Next, we used the RADD model to introduce an electrophilic moiety to the triazolopyridine scaffold such that it would selectively react with an active-site residue in AAA proteins. Targeted electrophilic compounds can form covalent bonds with proximal cysteine residues only when non-covalent interactions are already formed with the protein[20]. However, no cysteine directly interacts with the adenine base of the nucleotide bound to katanin. Guided by the RADD model, we identified Asp-210 as a solvent-accessible amino acid side chain predicted to be proximal to the bound triazolopyridine scaffold (distance of ~4.9 Å between the compound 2-nitrogen to the Asp-210 β-carbon, Fig. 3a). Sequence alignments of the ATP-binding sites of 32 human AAA proteins (~one-third of the AAA protein genes in humans) revealed that an Asp residue equivalent to Asp-210 in katanin is conserved in ~60% of the sites examined. A few AAA proteins (~9%) have a Ser residue at this site; however, we found no native cysteine (Extended Data Fig. 2a,b). We hypothesized that, as a Ser residue is accommodated, a mutation to Cys may be biochemically silent and could sensitize an AAA protein to an allele-specific covalent inhibitor[21].

To test this, we designed an ATPase-active katanin construct (aa 111–491; hereafter katanin-WT) and mutated Asp-210 to cysteine (katanin-D210C, Fig. 3b and Extended Data Fig. 2c). Unlike the kata-AAA constructs, which are expected to be inactive ATPases based on our studies of the related AAA protein spastin[14], these longer constructs are likely to retain ATP hydrolysis activity. Next, we characterized the nucleotide binding and kinetic parameters using DSF and steady-state ATPase assays, respectively, for both katanin-WT and katanin-D210C (Fig. 3c and Extended Data Fig. 2d). We did not observe a substantial difference between the two enzymes (ΔT_m, 4.5–5.5 °C for katanin-WT versus 4.5–4.8 °C for katanin-D210C in the presence of 1 mM ADP, range, $n = 2$) ($K_{1/2} = 0.25$ versus 0.26 mM, ranges 0.23–0.28 and 0.23–0.30 mM, and $k_{cat} = 4.9$ versus 5.0 s^{-1}, ranges 4.2–5.6 and 4.7–5.3 s^{-1}, for the WT and D210C mutant, respectively, average values, $n = 2$).

We next synthesized compound **5** (Fig. 3d and Supplementary Note 2), in which a phenyl-3-acrylamide group was added to the C2 amino of compound **2**, the highest affinity kata-AAA ligand we identified (Fig. 2c), so as to direct reactivity of the electrophile to the engineered cysteine. We first tested binding of compound **5** to katanin using DSF. Gratifyingly, the melting temperature of katanin-D210C increased by 11.8–12.3 °C in the presence of **5**, whereas the melting temperature of katanin-WT was increased by 4.8–6.3 °C (50 µM compound **5**, range, $n = 2$, Fig. 3e). Consistent with irreversible covalent inhibition, the ATPase activity of katanin-D210C was time-dependent (Fig. 3f). With 20 min incubation, compound **5** resulted in a dose-dependent inhibition (IC_{50} of 13 ± 3 nM, mean ± s.d., $n = 3$, 1 mM ATP) of the engineered mutant. Importantly, >900-fold selectivity was observed for the mutant allele compared to the WT katanin (Fig. 3g).

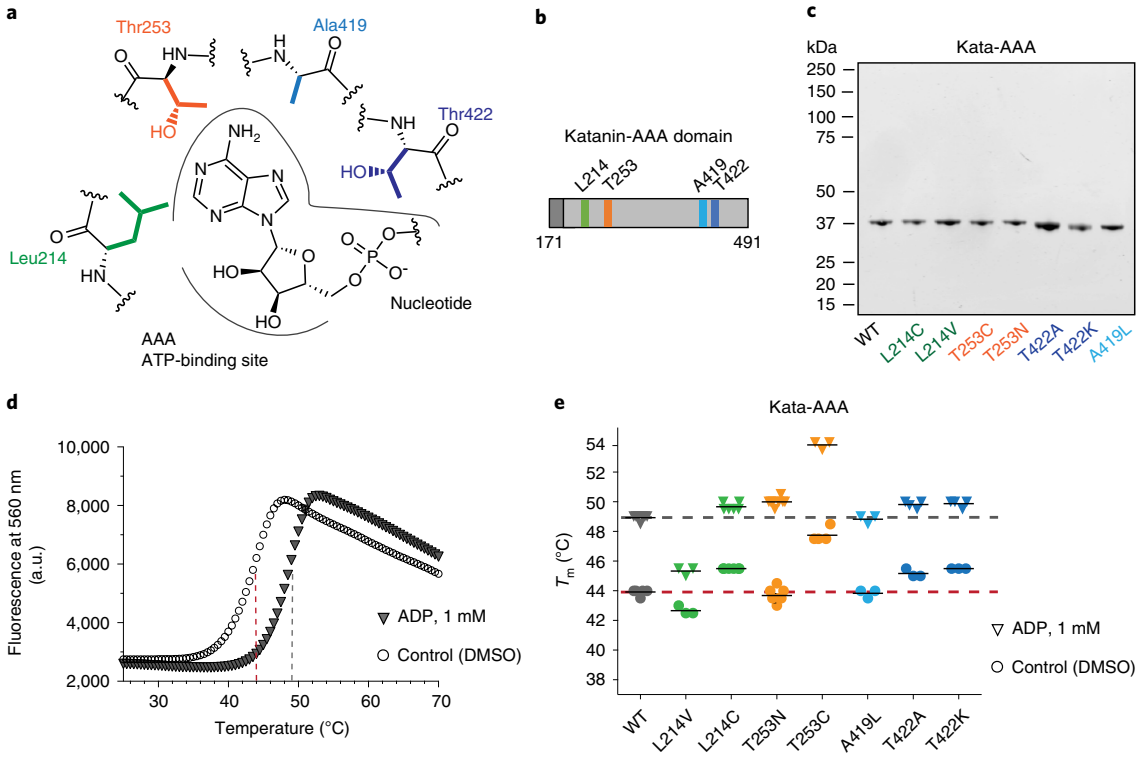

Fig. 1 | Engineering biochemically silent mutations in the ATP-binding site of katanin. a, Schematic showing variability hotspot residues in the katanin nucleotide-binding site. **b**, Schematic showing the AAA domain (light gray box, not to scale), the first and last residues, and the residues that were mutated in katanin's AAA domain (bars, colored as in **a**). **c**, SDS–PAGE gel of purified WT and mutant human katanin AAA domain (aa 171–491, Coomassie blue staining). **d**, DSF traces for katanin AAA domain WT in the presence or absence of ADP (1 mM) (5% DMSO in both conditions). Dashed lines indicate inflection points. **e**, Thermal stability of WT and mutant katanin AAA domain constructs analyzed using DSF. The graph shows melting temperatures (T_m) (colored as in **a**, with WT in gray) in the absence (triangles) and presence (circles) of ADP (1 mM), with mean values indicated by black bars ($n \geq 3$ independent experiments). Mean T_m values for WT are indicated by dashed lines (red, control; gray, ADP; $n = 3$ independent experiments). The unprocessed gel image for **c** and data for graphs in **d**,**e** are available as source data.

We further tested our binding model by designing two katanin constructs with engineered Cys mutations in the ATP-binding pocket in positions distinct from Asp210. For these experiments we used an ATPase-active *Xenopus laevis* katanin construct (~93% identical to human katanin in the AAA domain) that we published previously[13]. We note that the L211 and T250 residues in the *X. laevis* construct correspond to L214 and T253 in the human katanin construct. For the L211C and T250C mutants, we found no substantial inhibition in the presence of **5** (Fig. 3h and Extended Data Fig. 2e). Also, compound **5** does not inhibit a recombinant form of VCP/p97, which contains a native cysteine in the active site at a position different from the human katanin Cys-210 residue[22] (Fig. 3h). Together, these data indicate that the non-covalent interactions made by the compound impart specificity by inducing reactivity with a proximal cysteine with a suitable relative orientation. We name compound **5** 'allele-specific, proximity-induced reactivity-based inhibitor-1' (ASPIR-1) (Fig. 3d).

Probing katanin function with the allele-specific inhibitor. A compound for which katanin is the proposed cellular target has been reported[23]. However, direct binding by the inhibitor to this AAA protein has not been demonstrated, and no selective katanin inhibitors that can be used to probe its function are known. To investigate the utility of ASPIR-1 as a chemical probe for katanin's cellular function, we generated matched cell lines expressing either an N-terminal enhanced green fluorescent protein (EGFP)-tagged WT (inhibitor-insensitive, hereafter kata-WT) or D210C full-length katanin alleles (inhibitor-sensitive, hereafter kata-D210C) using a Flp-In system. Western blot analyses indicate that tagged WT and D210C proteins are expressed at levels approximately six- to eight-fold higher than endogenous katanin (Fig. 4a and Extended Data Fig. 3a). Live-cell fluorescence confocal microscopy showed that both EGFP-tagged katanin-WT and D210C mutant concentrate at the spindle poles during cell division, but distribute in the cytoplasm during interphase with some accumulation at puncta that are probably centrosomes, consistent with other studies[24] (Extended Data Fig. 3b,c).

Katanin interacts with CAMSAP2, a protein that binds to the microtubule lattice formed by minus-end polymerization and regulates microtubule dynamics[25–27] (Fig. 4b). We used immunofluorescence to examine CAMSAP2 localization to interphase microtubules in DMSO-treated kata-WT and kata-D210C cells, and found that it forms ~1 µm stretches (Fig. 4c). Comparing the lengths of CAMSAP2 stretches revealed minimal difference between DMSO-treated kata-WT and kata-D210C cells (stretch length 1.1 ± 0.5 µm for kata-WT versus 1.2 ± 0.5 µm for kata-D210C, mean ± s.d., 341 stretches measured in $n = 17$ kata-WT cells and 384 stretches measured in $n = 15$ kata-D210C cells, Fig. 4d,f,g).

Treatment with ASPIR-1 increased the average length of CAMSAP2 stretches in kata-D210C cells (1.7 ± 0.7 µm, mean ± s.d., 429 stretches measured in 20 cells, 1.25 µM compound, 4-h treatment), but had no significant effect in kata-WT cells (1.2 ± 0.5 µm, mean ± s.d., 420 stretches measured in 22 cells) (Fig. 4e–g). The magnitude of the change in the CAMSAP2 stretch length in kata-D210C cells is comparable to what has previously been observed with katanin knockdown (approximately twofold)[27]. Consistently, in

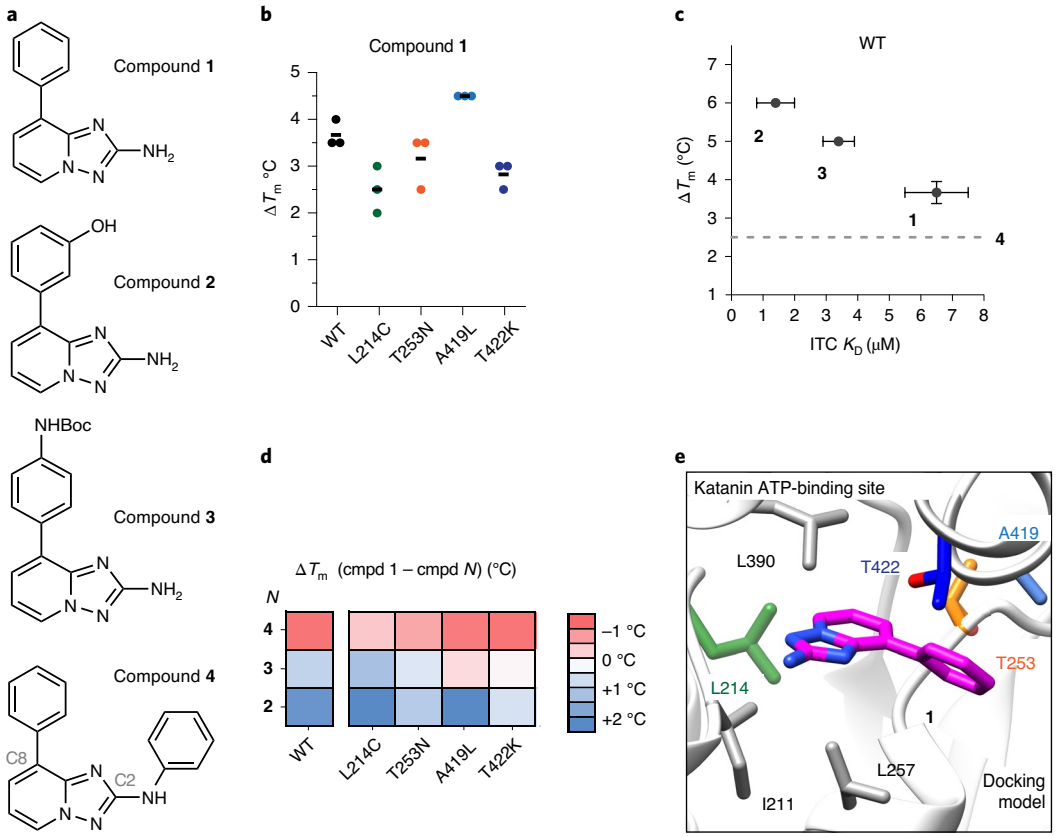

Fig. 2 | Using RADD to analyze the binding of triazolopyridine-based compounds to katanin. a, Chemical structures of compounds **1**–**4**. **b**, Graph showing the difference in T_m values (ΔT_m) in the presence of compound **1** (500 μM) versus control (DMSO) for katanin AAA domain WT and four mutant constructs ($n = 3$ independent experiments, black bar indicates mean). **c**, Relationship between ΔT_m and dissociation constants (K_D) measured by ITC for compounds **1**–**3** (500 μM). For compound **4**, K_D could not be measured, and the dashed line indicates ΔT_m. For ΔT_m, data represent mean ± s.d. for compound **1** ($n = 3$ independent experiments) and mean ± range for compounds **2** and **3** ($n = 2$ independent experiments). For K_D, data represent fitted values and error bars denote fitting error (one experiment). **d**, Effect of katanin AAA domain mutations on the structure–activity relationship of triazolopyridine-based compounds. The heat map was built using the difference between the average ΔT_m for compound **1** and that for analogs **2**–**4**, determined for each indicated construct. **e**, RADD model for compound **1** (purple and blue, stick representation) bound to katanin (gray, ribbon representation). Variability hotspot residues are shown (stick representation, color-coded as in Fig. 1a). Other key amino acids in the katanin nucleotide-binding site are also shown (gray, stick representation). The image was generated using UCSF Chimera. Additional models are shown in Extended Data Fig. 2c. The data for graphs in **b**–**d** are available as source data.

the presence of increasing concentrations of ASPIR-1, a shift in the frequency distribution of CAMSAP2 stretch lengths was observed in kata-D210C cells, but not in kata-WT cells ($P < 0.001$, Kruskal–Wallis test with Dunn's multiple comparisons correction, Fig. 4f,g). Notably, ASPIR-1-treated kata-D210C cells showed more CAMSAP stretches with lengths >2.5 μm compared to kata-WT cells (62–90 stretches out of 429–785 total measured versus 11–17 out of 420–621, Fig. 4f,g). We also evaluated the cytotoxicity of ASPIR-1 in kata-WT cells and found no substantial reduction in viability up to 5 μM concentration (Extended Data Fig. 3d). Furthermore, at an equivalent concentration to that used for the CAMSAP2 staining experiments (1.25 μM), we did not detect any broad morphological alteration of the microtubule cytoskeleton, suggesting that ASPIR-1 does not generally disrupt microtubule dynamics (Extended Data Fig. 3e). Together, these data indicate that the covalent katanin inhibitor can phenocopy RNAi-mediated katanin depletion and that katanin's ATPase activity regulates CAMSAP2 localization at microtubule minus ends in interphase cells.

Engineering inhibitor-sensitive alleles of FIGL1 and VPS4B. To examine the broader applicability of the allele-specific inhibitor design approach, we focused on VPS4B and FIGL1—AAA proteins required for membrane remodeling and the homologous recombination pathway of DNA repair, respectively[5,28]. No inhibitor for FIGL1 has been reported, and although two VPS4 inhibitors have been described, VCP/p97 is a known additional target of these compounds, limiting their utility as probes in cells[22,29]. We generated a tag-free recombinant human FIGL1 construct (aa 296–695), used an established procedure to purify human VPS4B (full-length) with N-terminal 6×His and SUMO tags (hereafter, HS-VPS4B)[13], and tested their ATPase activity in the presence of ASPIR-1 (Extended Data Fig. 4a). Gratifyingly, ASPIR-1 does not inhibit WT HS-VPS4B or FIGL1 constructs (5 μM ASPIR-1, 1 mM ATP, 30 min incubation; Extended Data Fig. 4b).

Both VPS4B and FIGL1 contain an Asp residue at a position equivalent to that of Asp-210 in katanin. Therefore, we generated alleles with the corresponding Asp-to-Cys mutations (hereafter HS-VPS4B-D135C and FIGL1-D402C, Extended Data Fig. 4a). Next, we analyzed the ATPase activities of the engineered cysteine mutants. Both mutant constructs have $K_{1/2}$ values within ~1.5-fold of the corresponding WT constructs (Fig. 5a,b and Extended Data Fig. 4c,d). Consistently, ADP binding increases the thermal stability of WT and Asp-to-Cys mutants to a similar extent (approximately +5 °C for VPS4B and +3 °C for FIGL1, Extended Data Fig.

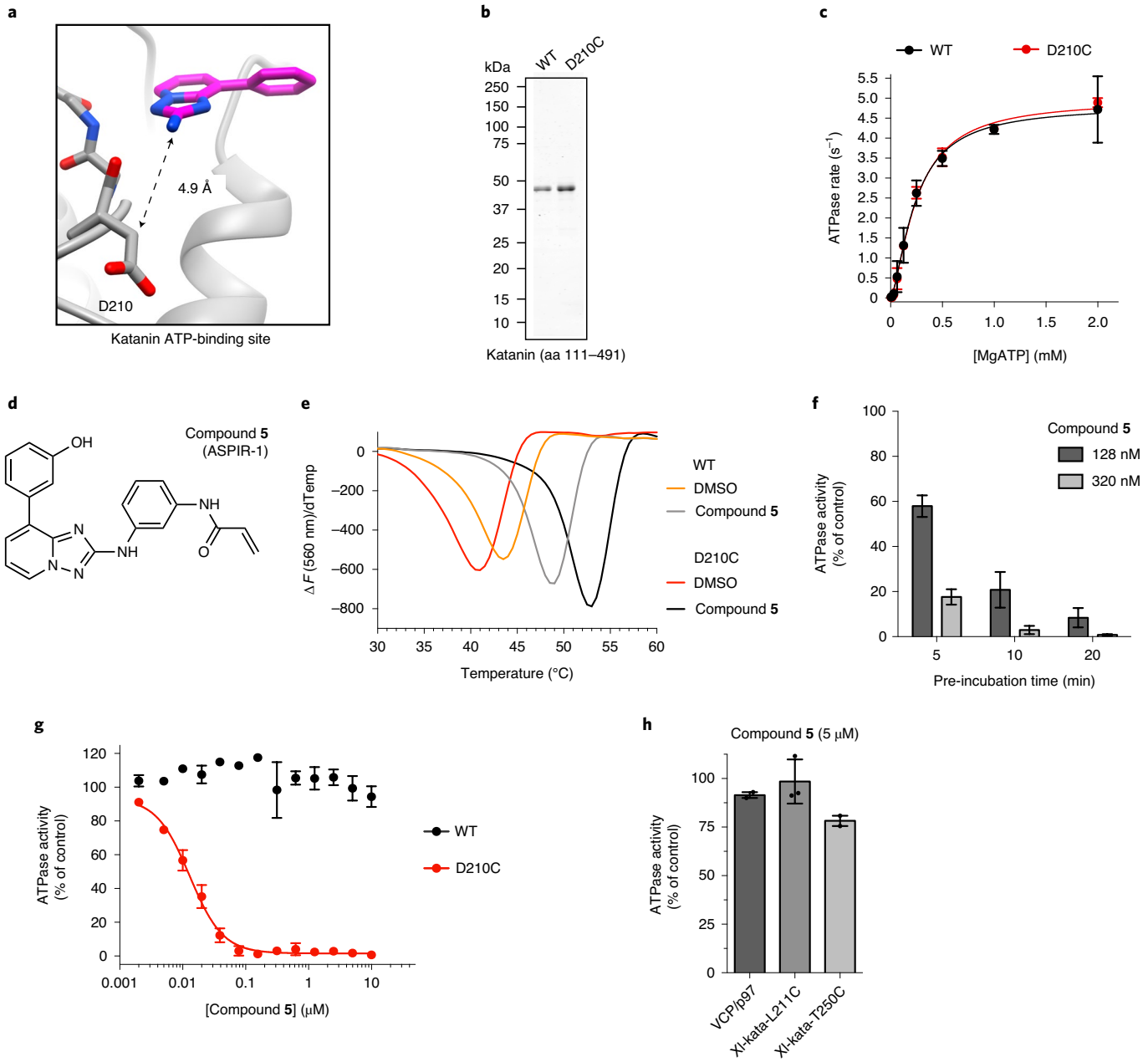

Fig. 3 | Design of an allele-specific covalent inhibitor of katanin. a, RADD model for compound **1** (purple and blue stick representation) bound to katanin (ribbon and stick representation), indicating the distance between the 2-nitrogen atom of compound **1** and the β-carbon of residue D210. **b**, SDS–PAGE gel of purified recombinant human katanin-WT and katanin-D210C (aa 111–491; Coomassie blue staining). **c**, ATP concentration dependence of the steady-state activity of WT and D210C mutant katanin, analyzed using an NADH-coupled assay. Rates were fit to the Michaelis–Menten equation for cooperative enzymes (mean ± range, $n = 2$ independent experiments). **d**, Structure of compound **5** (ASPIR-1). **e**, DSF analysis of compound **5**-dependent changes in the melting temperatures of katanin-WT and katanin-D210C (50 μM compound **5**, $n = 2$ independent experiments). One representative experiment is shown. **f**, Time-dependent inhibition of the steady-state ATPase activity of katanin-D210C by compound **5** (1 mM ATP). The graph shows percentage residual ATPase activity (mean ± range, $n = 2$ independent experiments). **g**, Concentration-dependent inhibition of the steady-state ATPase activity of WT and D210C katanin by compound **5** (1 mM ATP, 20 min incubation). Graph shows percentage residual ATPase activity values relative to DMSO control fit to a sigmoidal dose–response equation (mean ± s.d., $n = 3$ independent experiments for katanin-D210C; mean ± range, $n = 2$ independent experiments for katanin-WT). **h**, Percentage residual ATPase activity of VCP/p97 (WT) and *X. laevis* katanin (L211C and T250C mutants) in the presence of compound **5** (mean ± range, $n = 2$ independent experiments for VCP/p97 and *X. laevis* katanin T250C; mean ± s.d., $n = 3$ independent experiments for *X. laevis* katanin L211C). The unprocessed gel image for **b** and data for graphs in **c** and **e**–**h** are available as source data.

4e,f). Catalytic efficiency was reduced approximately twofold for FIGL1-D402C and approximately sixfold for HS-VPS4B-D135C with respect to the WT constructs (Fig. 5c,d and Extended Data Fig. 4c,d). Thus, the Cys mutant alleles tested retain adenine nucleotide binding and ATPase activity.

Next, we examined whether ASPIR-1 could inhibit the cysteine-mutant alleles of these AAA proteins. Based on the overall similarity of the VPS4B and FIGL1 nucleotide-binding pockets compared to that of katanin, we anticipated that ASPIR-1 would adopt a similar pose and target the engineered cysteine

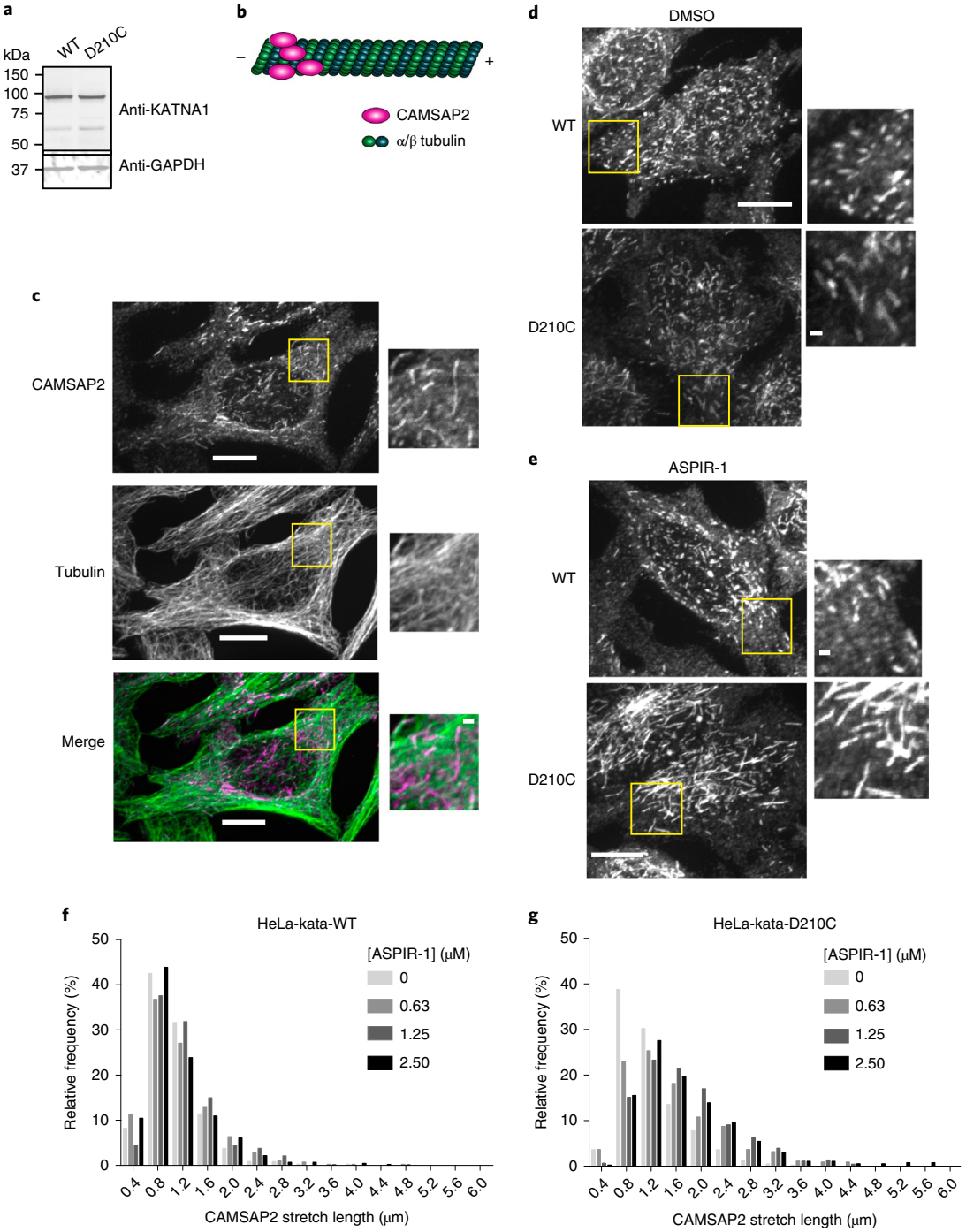

Fig. 4 | Probing katanin function using a covalent inhibitor and sensitized allele pair. a, Immunoblot analysis of HeLa cells expressing WT or mutant (D210C) N-terminal EGFP-tagged katanin constructs. **b**, CAMSAP2 decorates microtubule minus ends. **c**, Immunostaining for CAMSAP2 (magenta) and α-tubulin (green) in kata-WT cells. Scale bars, 10 μm. Enlarged portions of the areas in the yellow boxes are shown in the insets. Scale bars, 1 μm. Representative images are shown ($n = 3$ independent experiments, 10 images acquired per experiment). **d**–**g**, Effect of ASPIR-1 treatment on CAMSAP2 stretch length. Images show kata-WT and kata-D210C cells treated with DMSO (control, **d**) or ASPIR-1 (1.25 μM, **e**) and stained for CAMSAP2. Scale bars, 10 μm in primary images and 1 μm in insets. Representative images are shown ($n = 3$ independent experiments, 10 images acquired per condition per experiment). The graphs show the length distribution (relative frequency) of CAMSAP2 stretches in control (DMSO) and ASPIR-1-treated kata-WT (**f**) and kata-D210C cells (**g**) (0–2.5 μM ASPIR-1). The unprocessed gel image for **a** and data for graphs in **f**,**g** are available as source data.

residue. Gratifyingly, we found that ASPIR-1 inhibits both HS-VPS4B-D135C and FIGL1-D402C ATPase activity (IC_{50}: HS-VPS4B-D135C, 0.18 ± 0.05 μM; FIGL1-D402C, 0.56 ± 0.35 μM; mean ± s.d., $n \geq 3$, 1 mM ATP, 30-min incubation, Fig. 5e,f). Selectivity over the WT allele is at least 100-fold for VPS4B and at least 40-fold for FIGL1 under the same conditions (Fig. 5e,f). Direct binding assays using DSF also corroborated selective binding to the cysteine mutants (Fig. 5g,h). ASPIR-1 increases the thermal stability of both FIGL1 and HS-VPS4B-WT and Asp-to-Cys mutants, but has a much more pronounced effect on the mutant proteins than

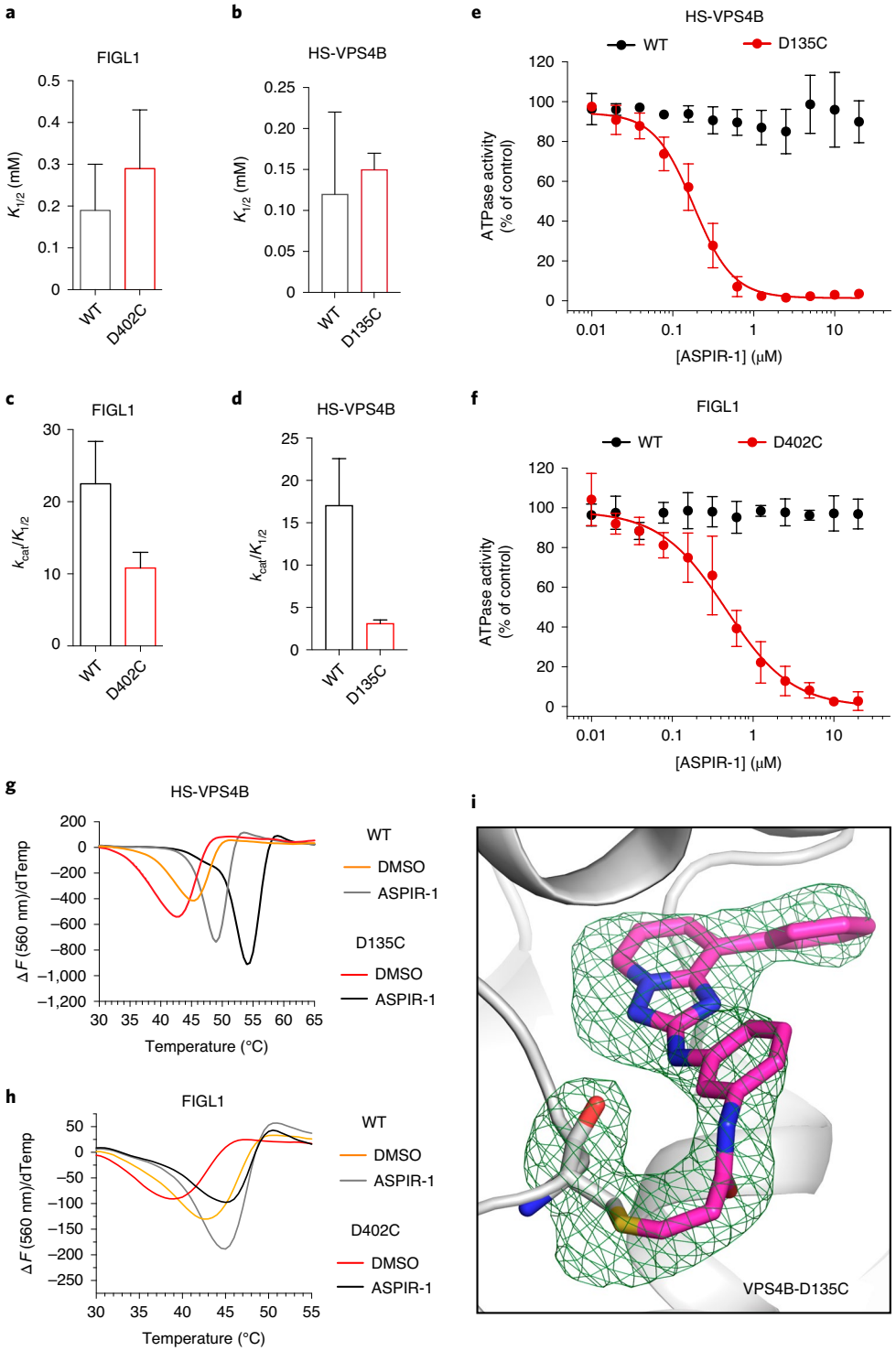

Fig. 5 | Allele-specific inhibition of the AAA proteins VPS4B and FIGL1. a–d, Effect of the inhibitor-sensitizing mutation on the enzymatic activities of HS-VPS4B and FIGL1. Graphs show values for the ATP concentration required for the half-maximal velocity ($K_{1/2}$; **a**,**b**) and catalytic efficiency ($k_{cat}/K_{1/2}$; **c**,**d**) of WT and D-to-C mutant HS-VPS4B and FIGL1 constructs, analyzed by measuring the steady-state ATPase rate across a range of ATP concentrations using an NADH-coupled assay (mean ± s.d., $n = 3$ independent experiments for HS-VPS4B-WT and HS-VPS4B-D135C, $n = 5$ for FIGL1-WT and $n = 7$ for FIGL1-D402C). **e**,**f**, Concentration-dependent inhibition of the steady-state ATPase activity of WT and D135C HS-VPS4B (**e**) or WT and D402C FIGL1 (**f**) by ASPIR-1 (1 mM ATP, 30-min incubation). Graphs show percentage residual ATPase activity values relative to DMSO control (mean ± s.d., $n = 3$ independent experiments for HS-VPS4B-WT, HS-VPS4B-D135C and FIGL1-WT, $n = 5$ for FIGL1-D402C). Data for HS-VPS4B-D135C and FIGL1-D402C were fit to a sigmoidal dose–response equation. **g**,**h**, DSF analysis of ASPIR-1-dependent changes in the melting temperatures of WT and D135C HS-VPS4B (**g**) or WT and D402C FIGL1 (**h**). Melting temperatures in the presence of ASPIR-1 (50 μM) for HS-VPS4B-WT: DMSO = 45.1 °C (range 45.0–45.3 °C), ASPIR-1 = 49.0 °C (no range); HS-VPS4B-D135C: DMSO = 42.5 °C (no range), ASPIR-1 = 54.0 °C (no range); FIGL1-WT: DMSO = 42.8 °C (range 42.5–43.0 °C), ASPIR-1 = 44.5 °C (no range); FIGL1-D402C: DMSO = 39 °C (no range), ASPIR-1 = 45.0 °C (no range) ($n = 2$ independent experiments). One representative experiment is shown. **i**, Crystal structure of ASPIR-2 (stick representation) bound to VPS4B-D135C (ribbon and stick representation). A simulated annealing omit map of ASPIR-2 and Cys-135 contoured to 3.0σ is shown as a green mesh. The data for graphs in **a**–**h** are available as source data.

Table 1 | Data collection and refinement statistics

	VPS4B-D135C/ASPIR-2[a] (PDB 7L9X)
Data collection	
Space group	*P*65
Cell dimensions	
a, *b*, *c* (Å)	77.88, 77.88, 132.83
α, β, γ (°)	90.00, 90.00, 120.00
Resolution (Å)	29.24–2.81 (2.87–2.81)[b]
R_{sym} or R_{merge}	0.02234 (0.3546)
$I/\sigma I$	14.62 (1.19)
Completeness (%)	98.72 (88.90)
Redundancy	2.0 (1.9)
Refinement	
Resolution (Å)	29.24–2.81
No. reflections	10,978
R_{work} / R_{free}	0.209 / 0.267
No. atoms	
Protein	2,261
Ligand/ion	32
Water	33
B factors	
Protein	95.10
Ligand/ion	76.39
Water	82.43
R.m.s. deviations	
Bond lengths (Å)	0.004
Bond angles (°)	0.71

[a]1 crystal used. [b]Values in parentheses are for the highest-resolution shell.

on the WT proteins (+11.5 °C for HS-VPS4B-D135C versus +4.0 °C for HS-VPS4B-WT, and +6 °C for FIGL1-D402C versus +2.0 °C for FIGL1-WT, Fig. 5g,h). Thus, in three AAA proteins, sensitivity to inhibition with ASPIR-1 can be engineered by introducing a cysteine residue at a specific position in the ATP-binding site.

To examine the mechanism of inhibition of the AAA alleles by ASPIR-1 we employed X-ray crystallography. Many crystal structures have been reported for VPS4 but relatively few for katanin and FIGL1 (example VPS4 PDB entries: 1XWI, 2QPA, 2QP9, 3EIH, 3EIE). Therefore, for these experiments we focused on VPS4 and generated a tag-free WT (hereafter VPS4B-WT) construct, which has been previously used for crystallography[30], and the corresponding VPS4B-D135C mutant (Extended Data Fig. 5a). We found that VPS4B-WT was substantially less active than the tagged construct, and therefore examined its ATPase activity in the presence of recombinant purified VTA1, a known VPS4 activator (Extended Data Fig. 5a)[31,32]. VPS4B-D135C has a $K_{1/2}$ value approximately fourfold higher and a k_{cat} value approximately twofold lower than the WT protein ($K_{1/2}$ = 14 versus 60 µM, ranges 13–15 and 56–63 µM, and k_{cat} = 2.5 versus 1.2 s^{-1}, ranges 2.1–3.0 and 1.1–1.3 s^{-1}, for the WT and D135C mutant, respectively, n = 2, Extended Data Fig. 5b). Gratifyingly, we obtained crystals of VPS4B-D135C in the presence of ASPIR-2, an analog of ASPIR-1 that lacks the phenolic hydroxyl group (Extended Data Fig. 5c; ASPIR-2 synthesis is described in Supplementary Note 2). We determined the structure at a resolution of ~2.8 Å using molecular replacement as described in the Methods (Table 1, PDB 7L9X). Similar to ASPIR-1, ASPIR-2 inhibits VPS4B-D135C in a time- and dose-dependent manner (IC_{50} = 410 nM, range 300–510 nM, n = 2, 30-min incubation, 1 mM ATP; Extended Data Fig. 5d,e). The structure indicates that ASPIR-2 occupies the nucleotide-binding site and, importantly, a simulated annealing omit map confirms electron density connecting the Cys-135 residue and the ASPIR-2 acrylamide moiety, consistent with covalent bond formation (Fig. 5i and Extended Data Fig. 5f). Moreover, ASPIR-2 binds VPS4B-D135C in a pose that overlays with our RADD binding model for the triazolopyridine scaffold in the nucleotide-binding site (Extended Data Fig. 5g). Together, these data reveal how proximity-induced reactivity can lead to allele-specific chemical inhibition of an AAA protein.

Discussion

Here, we report the design of ASPIR-1, a compound that selectively inhibits AAA alleles with a cysteine mutation. An X-ray structure of an ASPIR-1 analog bound to the VPS4B cysteine-mutant allele verifies our RADD model for inhibitor design and suggests how proximity-induced reactivity-based selectivity can be achieved (Fig. 6). ASPIR-1 is a selective and cell-active inhibitor that may be used to probe the functions of katanin, FIGL1 and VPS4B, three AAA proteins with key roles in processes as diverse as microtubule cytoskeleton organization, DNA repair and membrane remodeling. We anticipate that ASPIR-1 will also be useful for probing the cellular functions of other AAA proteins.

The finding that ASPIR-1 can selectively inhibit engineered alleles of three AAA proteins, which belong to the classic clade of the AAA protein family[2], can be explained by their structural and sequence similarity. At the four variability hotspot residues in the AAA nucleotide-binding site, which our previous studies identify as important determinants of inhibitor binding[13], the only difference between katanin and VPS4B or FIGL1 is a single conservative substitution (Thr253 in katanin versus Ser181 for VPS4B; Leu214 in katanin versus Val406 for FIGL1). Therefore, it is likely that the non-covalent triazolopyridine scaffold makes similar interactions with all three proteins. For other closely related AAA proteins with similar subtle differences in the variability hotspot residues, such as the proteasome subunits[3], sensitization to ASPIR-1 inhibition should be feasible simply by introducing a cysteine at the equivalent position of the Asp residue mutated in this study. Chemical modifications of ASPIR-1 to improve binding to a different target protein may also be guided by alignments with our crystal structure. However, extending this approach to AAA proteins with substantially divergent variability hotspots will probably require identification of additional suitable fragments. Alternately, for more divergent AAA proteins, in addition to the electrophile-sensitizing cysteine, a second mutation may be introduced in a variability hotspot to generate an allele that binds triazolopyridine-based compounds. The data presented here and in previous work by us and others[9,13] indicate that these amino acid substitutions should be well-tolerated.

The fact that the non-covalent portion of the inhibitor binds AAA proteins independently of the covalent group, albeit with low affinity, should allow pharmacological properties, such as specificity, target occupancy and inhibitor residence time, to be tailored to specific chemical biology studies of the AAA protein family by modification of the electrophile-cysteine interaction[33]. Our data show that ASPIR-1, which has an acrylamide electrophile, can achieve nearly stoichiometric inactivation of the target AAA protein with short incubation times (20–30 min, in vitro, at room temperature). Such rapid inactivation could be particularly useful to dissect AAA function in dynamic cellular processes that occur within this timescale, such as VPS4-mediated organelle biogenesis[5]. In cases where reactivation of the target AAA protein function may be desirable over irreversible inhibition, for example, when an AAA protein's functions in different processes are separated in time, reversible covalent inhibitors could be obtained using α-cyano-substituted

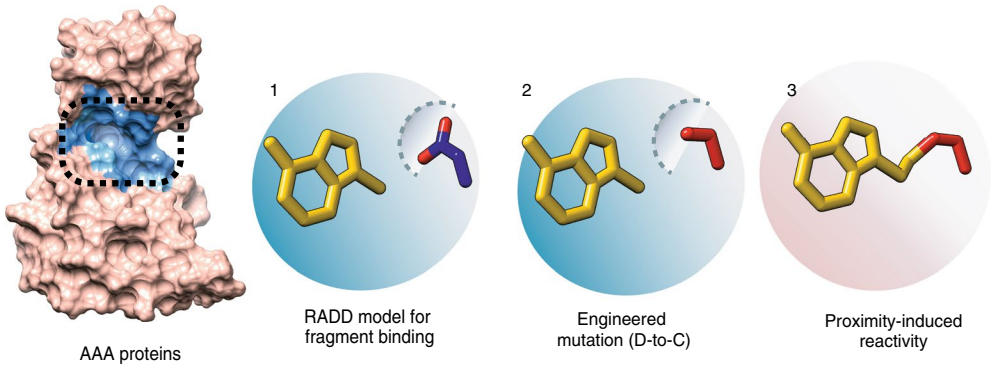

Fig. 6 | An approach for developing allele-specific covalent inhibitors for proteins in the AAA family. Schematic for the approach. (1) RADD is used to generate a binding model of a low-affinity fragment that binds conserved motifs in the AAA protein family. (2) This model guides the introduction of a biochemically silent cysteine mutation and (3) a functional group with proximity-induced reactivity is incorporated to generate a potent and selective covalent inhibitor for the engineered target protein allele.

acrylamides[34]. As the targeted engineered cysteine is located in an unhindered and solvent-accessible position, we expect that it should retain reactivity toward a diverse set of electrophiles.

Although our approach requires mutations to be introduced in the target, this can be relatively straightforward using CRISPR-Cas9 based gene-editing technologies[35]. We note that, in some cases, expression of the edited variant gene as the only AAA protein allele may not be necessary, because our data show that ASPIR-1 can phenocopy katanin RNAi-based gene knockdown when the mutant protein is expressed in the presence of the WT allele. Importantly, this experimental set-up could allow analyses of the functions of specific isoforms. For example, at least five isoforms of katanin-like 2, a risk gene for autism spectrum disorders, can be expressed in human cells[36,37]; however, the biological differences of these isoforms are presently unclear. We note that the engineered cysteine mutation can alter the ATPase activity of some AAA proteins more substantially than others (for example, catalytic efficiency is sixfold lower for mutant compared to WT for VPS4, but is essentially unchanged for katanin). If the expression of the mutant allele results in cellular phenotypes, the structural data for the inhibitor-protein binding may guide additional mutations to address this potential limitation, as has been required for other enzyme classes for which a similar chemical genetics approach has been developed[38].

More broadly, as AAA proteins' catalytic activities direct the assembly, disassembly and maturation of a variety of macromolecular complexes[1,5–7], the ability to inactivate AAA proteins in native environments could bring new insights into how transient intermediates of these protein complexes, along with their latent biological functions, are regulated. Finally, our chemical genetics approach also provides a valuable resource to test hypotheses for the development of new therapeutics targeting AAA proteins. Synthetic lethal interactions have been associated with the loss of one of the two VPS4 orthologs in certain colorectal and pancreatic cancer cell lines and with the loss of FIGL1 in cancer cells exposed to DNA-damaging agents[39,40]. Moreover, correlation between certain features of clinical cancer samples, such as high mTORC1 activity or chromosomal instability, with high expression levels of the AAA proteins RUVBL1/2 or TRIP13, respectively, suggests that inhibiting these proteins could lead to selective cancer cell death[41,42]. As other AAA proteins are suggested as new therapeutic targets, our approach could be extended to these proteins, which are all identified by their conserved AAA nucleotide-binding site, enabling accelerated examination of their pharmacological inhibition in relevant contexts.

Online content

Any methods, additional references, Nature Research reporting summaries, source data, extended data, supplementary information, acknowledgements, peer review information; details of author contributions and competing interests; and statements of data and code availability are available at https://doi.org/10.1038/s41594-021-00575-9.

Received: 18 November 2020; Accepted: 18 February 2021;
Published online: 29 March 2021

References

1. Puchades, C., Sandate, C. R. & Lander, G. C. The molecular principles governing the activity and functional diversity of AAA proteins. *Nat. Rev. Mol. Cell Biol.* **21**, 43–58 (2020).
2. Seraphim, T. V. & Houry, W. A. AAA proteins. *Curr. Biol.* **30**, R251–R257 (2020).
3. Gates, S. N. & Martin, A. Stairway to translocation: AAA+ motor structures reveal the mechanisms of ATP-dependent substrate translocation. *Protein Sci.* **29**, 407–419 (2020).
4. Wendler, P., Ciniawsky, S., Kock, M. & Kube, S. Structure and function of the AAA nucleotide binding pocket. *Biochim. Biophys. Acta Mol. Cell Res.* **1823**, 2–14 (2012).
5. McCullough, J., Frost, A. & Sundquist, W. I. Structures, functions, and dynamics of ESCRT-III/Vps4 membrane remodeling and fission complexes. *Annu. Rev. Cell Dev. Biol.* **34**, 85–109 (2018).
6. Roll-Mecak, A. & McNally, F. J. Microtubule-severing enzymes. *Curr. Opin. Cell Biol.* **22**, 96–103 (2010).
7. Bleichert, F., Botchan, M. R. & Berger, J. M. Mechanisms for initiating cellular DNA replication. *Science* **355**, eaah6317 (2017).
8. Assimon, V. A. et al. CB-6644 is a selective inhibitor of the RUVBL1/2 complex with anticancer activity. *ACS Chem. Biol.* **14**, 236–244 (2019).
9. Anderson, D. J. et al. Targeting the AAA ATPase p97 as an approach to treat cancer through disruption of protein homeostasis. *Cancer Cell* **28**, 653–665 (2015).
10. Bishop, A. C., Buzko, O. & Shokat, K. M. Magic bullets for protein kinases. *Trends Cell Biol.* **11**, 167–172 (2001).
11. Islam, K. The bump-and-hole tactic: expanding the scope of chemical genetics. *Cell Chem. Biol.* **25**, 1171–1184 (2018).
12. Zhou, H.-J. et al. Discovery of a first-in-class, potent, selective and orally bioavailable inhibitor of the p97 AAA ATPase (CB-5083). *J. Med. Chem.* **58**, 9480–9497 (2015).
13. Cupido, T., Pisa, R., Kelley, M. E. & Kapoor, T. M. Designing a chemical inhibitor for the AAA protein spastin using active site mutations. *Nat. Chem. Biol.* **15**, 444–452 (2019).
14. Pisa, R., Cupido, T., Steinman, J. B., Jones, N. H. & Kapoor, T. M. Analyzing resistance to design selective chemical inhibitors for AAA proteins. *Cell Chem. Biol.* **26**, 1263–1273 (2019).
15. Pisa, R. & Kapoor, T. M. Chemical strategies to overcome resistance against targeted anticancer therapeutics. *Nat. Chem. Biol.* **16**, 817–825 (2020).
16. Chou, T.-F. & Deshaies, R. J. Development of p97 AAA ATPase inhibitors. *Autophagy* **7**, 1091–1092 (2011).

17. Pisa, R., Cupido, T. & Kapoor, T. M. Designing allele-specific inhibitors of spastin, a microtubule-severing AAA protein. *J. Am. Chem. Soc.* **141**, 5602–5606 (2019).
18. Tang, W. K., Odzorig, T., Jin, W. & Xia, D. Structural basis of p97 inhibition by the site-selective anticancer compound CB-5083. *Mol. Pharmacol.* **95**, 286–293 (2019).
19. Niesen, F. H., Berglund, H. & Vedadi, M. The use of differential scanning fluorimetry to detect ligand interactions that promote protein stability. *Nat. Protoc.* **2**, 2212–2221 (2007).
20. Lagoutte, R., Patouret, R. & Winssinger, N. Covalent inhibitors: an opportunity for rational target selectivity. *Curr. Opin. Chem. Biol.* **39**, 54–63 (2017).
21. Garske, A. L., Peters, U., Cortesi, A. T., Perez, J. L. & Shokat, K. M. Chemical genetic strategy for targeting protein kinases based on covalent complementarity. *Proc. Natl Acad. Sci. USA* **108**, 15046–15052 (2011).
22. Magnaghi, P. et al. Covalent and allosteric inhibitors of the ATPase VCP/p97 induce cancer cell death. *Nat. Chem. Biol.* **9**, 548–556 (2013).
23. Kuo, T.-C. et al. Purine-type compounds induce microtubule fragmentation and lung cancer cell death through interaction with katanin. *J. Med. Chem.* **59**, 8521–8534 (2016).
24. Cheung, K. et al. Proteomic analysis of the mammalian Katanin family of microtubule-severing enzymes defines Katanin p80 subunit B-like 1 (KATNBL1) as a regulator of mammalian Katanin microtubule severing. *Mol. Cell. Proteomics* **15**, 1658–1669 (2016).
25. Hendershott, M. C. & Vale, R. D. Regulation of microtubule minus-end dynamics by CAMSAPs and patronin. *Proc. Natl Acad. Sci. USA* **111**, 5860–5865 (2014).
26. Jiang, K. et al. Structural basis of formation of the microtubule minus-end-regulating CAMSAP–katanin complex. *Structure* **26**, 375–382 (2018).
27. Jiang, K. et al. Microtubule minus-end stabilization by polymerization-driven CAMSAP deposition. *Dev. Cell* **28**, 295–309 (2014).
28. Kumar, R., Duhamel, M., Coutant, E., Ben-Nahia, E. & Mercier, R. Antagonism between BRCA2 and FIGL1 regulates homologous recombination. *Nucleic Acids Res.* **47**, 5170–5180 (2019).
29. Pöhler, R. et al. A non-competitive inhibitor of VCP/p97 and VPS4 reveals conserved allosteric circuits in type I and II AAA ATPases. *Angew. Chem. Int. Ed.* **57**, 1576–1580 (2018).
30. Scott, A. et al. Structural and mechanistic studies of VPS4 proteins. *EMBO J.* **24**, 3658–3669 (2005).
31. Azmi, I. et al. Recycling of ESCRTs by the AAA-ATPase Vps4 is regulated by a conserved VSL region in Vta1. *J. Cell Biol.* **172**, 705–717 (2006).
32. Yang, D. & Hurley, J. H. Structural role of the Vps4-Vta1 interface in ESCRT-III recycling. *Structure* **18**, 976–984 (2010).
33. Strelow, J. M. A perspective on the kinetics of covalent and irreversible inhibition. *SLAS Discov.* **22**, 3–20 (2017).
34. Bradshaw, J. M. et al. Prolonged and tunable residence time using reversible covalent kinase inhibitors. *Nat. Chem. Biol.* **11**, 525–531 (2015).
35. Knott, G. J. & Doudna, J. A. CRISPR-Cas guides the future of genetic engineering. *Science* **361**, 866–869 (2018).
36. Dunleavy, J. E. M. et al. Katanin-like 2 (KATNAL2) functions in multiple aspects of haploid male germ cell development in the mouse. *PLoS Genet.* **13**, e1007078 (2017).
37. Neale, B. M. et al. Patterns and rates of exonic de novo mutations in autism spectrum disorders. *Nature* **485**, 242–245 (2012).
38. Zhang, C. et al. A second-site suppressor strategy for chemical genetic analysis of diverse protein kinases. *Nat. Methods* **2**, 435–441 (2005).
39. Ma, J. et al. FIGNL1 is overexpressed in small cell lung cancer patients and enhances NCI-H446 cell resistance to cisplatin and etoposide. *Oncol. Rep.* **37**, 1935–1942 (2017).
40. McDonald, E. R. III et al. Project DRIVE: a compendium of cancer dependencies and synthetic lethal relationships uncovered by large-scale, deep RNAi screening. *Cell* **170**, 577–592 (2017).
41. Shin, S. H. et al. Synthetic lethality by targeting the RUVBL1/2–TTT complex in mTORC1-hyperactive cancer cells. *Sci. Adv.* **6**, eaay9131 (2020).
42. Marks, D. H. et al. Mad2 overexpression uncovers a critical role for TRIP13 in mitotic exit. *Cell Rep.* **19**, 1832–1845 (2017).

Methods

Plasmids. Plasmids for expressing *Mus musculus* VCP/p97, *X. laevis* katanin-p60, *Homo sapiens* fidgetin-like 1 (FIGL1) and *H. sapiens* VPS4B have been described previously[13,14]. We obtained a plasmid containing *H. sapiens* katanin-p60 (codon-optimized for *Escherichia coli*) from J. Ross (UMass Amherst). To generate plasmids for expression of recombinant human katanin aa 171–491 (katanin AAA domain) and aa 111–491 (katanin), the corresponding nucleotide sequences were cloned into the pMAL-c5x vector using BamHI and EcoRI restriction sites. A PreScission protease cleavage site was added to the N terminus to enable tag removal. The final katanin constructs contain a non-native glycine residue at the N terminus. For the generation of cell lines, the full-length katanin open reading frame (RefSeq NM_0070444) was purchased from GenScript and subcloned into the pcDNA5.0/FRT/TO vector (Thermo Fisher) with an N-terminal EGFP tag using KpnI and NotI restriction sites. Vectors for katanin, FIGL1 and VPS4B mutants were generated by site-directed mutagenesis. The cDNA for human VTA1 (full length, NCBI RefSeq DQ893520.2) was PCR-amplified from the ORFeome collection and cloned into a pGEX6p1 vector using the BamHI and EcoRI restriction sites.

Recombinant protein expression and purification. The purifications of VCP/p97 and WT HS-VPS4B (VPS4B) have been described previously and *X. laevis* katanin-p60 mutants were purified as described previously for the WT protein[13]. The buffers used in the purification methods reported below are detailed in Supplementary Note 1. FIGL1 and human katanin constructs were expressed in *E. coli* Rosetta (DE3) pLysS cells (Merck, cat. no. 70954) grown in Miller's LB medium (LMM, Formedium, cat. no. LMM105). For all constructs, culture growth at 37 °C was monitored by measuring absorbance at 600 nm (A_{600}) and protein expression was induced at $A_{600} = 0.6–0.8$ with 0.5 or 1.0 mM IPTG (GoldBio). The cultures were grown at 18 °C for 12–16 h, pelleted and resuspended in lysis buffer (Buffer 1A for FIGL1, 2A for human katanin, 3A for HS-VPS4B, 4A for VPS4B and 5A for VTA1). All subsequent purification steps were performed at 4 °C. Cell lysis was carried out using an EmulsiFlex-C5 homogenizer (Avestin, 5–6 cycles at 10,000–15,000 psi). The homogenized lysate was clarified by centrifugation at 40,000 r.p.m. for 45–60 min using a Ti45 rotor in a Beckman Coulter Optima LE-80K ultracentrifuge.

For purification of FIGL1, the clarified lysate was loaded onto glutathione resin and incubated for 45 min. The resin was washed with 40 volumes of Buffer 1B, then 10 volumes of Buffer 1C. The resin was resuspended in four volumes of Buffer 1C, PreScission protease was added and the resin was incubated overnight. The eluate from the glutathione resin was collected, diluted 2.5-fold with Buffer 1D, and loaded onto a Q-trap column (GE Healthcare). The flow-through containing FIGL1 was concentrated using an Amicon Ultra 30K device (cat. no. UFC803024, Millipore-Sigma), filtered, and loaded into a Superdex 200 Increase column equilibrated in Buffer 1F. Fractions containing purified FIGL1 were pooled, frozen in liquid nitrogen and stored at −80 °C. The final FIGL1 construct (aa 288–674) contains a non-native Pro-Gly sequence at the N terminus.

For purification of human katanin, the clarified lysate was loaded onto an MBP-trap column (GE Healthcare). The column was washed with 30 volumes of Buffer 2B, then 2–5 volumes of Buffer 2C and eluted with Buffer 2C supplemented with 10 mM maltose. PreScission protease was added to the eluate and incubated overnight. The solution was loaded onto a Q-trap column (GE Healthcare) and eluted with a gradient of Buffer 2D. Fractions enriched in katanin were concentrated using an Amicon Ultra 30K device (cat. no. UFC803024, Millipore-Sigma), filtered, and loaded into a Superdex 200 16/60 column equilibrated in Buffer 2E1 for katanin AAA domain (WT and mutants) or Buffer 2E2 for katanin (WT and mutant). Fractions containing purified katanin were pooled, concentrated using an Amicon Ultra 30K device to 200–500 µM for the katanin AAA domain or to 50–150 µM for katanin, frozen in liquid nitrogen and stored at −80 °C.

For purification of human HS-VPS4B-D135C, the clarified lysate was loaded onto Ni-NTA resin and incubated for 1 h. The resin was washed with ~500 ml of Buffer 3B and then eluted with Buffer 3C. The solution was diluted 1:2 in Buffer 3D, loaded onto a Q-trap column (GE Healthcare) and eluted with a gradient of Buffer 3E. Fractions containing HS-VPS4B-D135C were then pooled, concentrated using an Amicon Ultra 30K device, filtered, and loaded into a Superdex 200 16/60 column (GE Healthcare) equilibrated with Buffer 3F. The fractions containing purified HS-VPS4B-D135C were pooled, concentrated using an Amicon Ultra 30K device to 30–100 µM, frozen in liquid nitrogen and stored at −80 °C.

For purification of human WT VPS4B and human untagged VPS4B-D135C, the clarified lysate was loaded onto Ni-NTA resin and incubated for 1 h. The resin was washed with ~500 ml of Buffer 4B and then eluted with Buffer 4C. The eluate was treated with ~50 µl of 3 mg ml^{-1} Ulp1 protease and dialyzed in Buffer 4D overnight. Protein was loaded onto a Q-trap column (GE Healthcare) pre-equilibrated with Buffer 4E, and eluted in a gradient of 0% to 100% Buffer 4F in 20 min. Fractions containing VPS4B protein were concentrated using an Amicon Ultra 30K concentrator to ~2 ml, filtered, and loaded into a Superdex 200 16/60 column (GE Healthcare) equilibrated with Buffer 4G. The fractions containing purified VPS4B were pooled, concentrated using an Amicon Ultra 30K device to 70–200 µM, and either frozen in liquid nitrogen and stored at −80 °C or used immediately for X-ray crystallography studies..

For purification of full-length human VTA1, the clarified lysate was loaded onto 2 ml of glutathione-agarose resin and incubated for 1 h. The resin was washed with ~500 ml of Buffer 5B and then eluted with Buffer 5C. The eluate was treated with ~50 µl of 3 mg ml^{-1} PreScission protease to cleave the N-terminal GST tag and dialyzed in Buffer 5D overnight. Protein was loaded onto a Q-trap column (GE Healthcare) pre-equilibrated with Buffer 5D, eluted in a 0% to 100% gradient of Buffer 5E in 20 min, concentrated using an Amicon Ultra 30K concentrator to ~2 ml, filtered, and loaded into a Superdex 200 16/60 column (GE Healthcare) equilibrated with Buffer 5F. The fractions containing purified VTA1 were pooled, concentrated using an Amicon Ultra 30K device to 150–200 µM, and flash-frozen in liquid nitrogen and stored at −80 °C.

Differential scanning fluorimetry. These experiments were carried out on a C1000 Touch Thermal cycler CFX-96 instrument (GE Healthcare). Compound solutions in DMSO (1 µl) were added to a 96-well plate (Hard-shell HSP9665 Bio-Rad), followed by 9 µl of assay buffer (20 mM HEPES.Na, 120 mM NaCl, 5 mM $MgCl_2$, 1 mM TCEP, 10 mM $(NH_4)_2SO_4$, pH 7.5) supplemented with SYPRO Orange (1:250 dilution, Thermo Fisher cat. no. S6651). Purified katanin, HS-VPS4B or FIGL1 constructs were diluted to 16 µM in assay buffer, and 10 µl was added to the plate (assay concentrations: compound, 50–500 µM; protein, 8 µM; DMSO, 5%). The temperature was linearly increased with a step of 0.5 °C for 55 min, from 25 °C to 95 °C, and fluorescence readings were taken at each interval (excitation 490 nm, emission 560 nm). Melting temperatures were calculated as the minimum value of the first derivative of the measured fluorescence versus temperature curves.

Compound docking. Simulations and docking calculations were performed using the Schrödinger Maestro program package (v. 12.2.02). Compound **1** was docked into katanin's ATP-binding site using PDB 5ZQM (chain A). For the generation of the docking grids, a cubic box (dimensions of 16 Å) was centered at the ATP-binding site. The cutoff for coulombic interactions was set to 0.25, and the scaling factor for van der Waals interaction was set at 0.9. For docking, the same cutoff was used for coulombic interactions and the scaling factor for van der Waals interactions was set to 0.8. The top 10 binding poses were analyzed, clustered in four different groups based on pose similarity, and one representative structure for each of the four groups was energy-minimized (shown in Extended Data Fig. 1c).

Isothermal titration calorimetry. ITC measurements were performed using a MicroCal auto-iTC200 calorimeter (MicroCal). Briefly, purified katanin-p60 AAA domain construct was dialyzed against HEPES.Na (20 mM), NaCl (150 mM), $MgCl_2$ (5 mM), $(NH_4)_2SO_4$ (10 mM), TCEP (1 mM), pH 7.5, for 6 or 9 h at 4 °C. DMSO solutions of compounds **1**, **2** or **3** were diluted in dialysis buffer (200 µM, 2.5% DMSO final) and titrated into a solution of the dialyzed protein (20 µM in dialysis buffer plus 2.5% DMSO, ~200 µl) in the ITC chamber. ITC titrations were carried out at 25 °C, while stirring at 275 r.p.m. An initial injection of 0.4 µl was followed by 19 injections of 2.0 µl of compound, with a duration of 4 s (per injection) and a spacing of 150 s. The heat of dilution was determined by independent titrations (buffer into protein) and was subtracted from the experimental data. The collected data were analyzed using AFFINImeter software and plotted using Prism (version 6.0, GraphPad Software). Dissociation constants from each titration were obtained using a single-site equilibrium-binding model.

Analysis of ATPase activity. The steady-state ATPase activities of katanin, FIGL1, VPS4B and VCP/p97 proteins were examined using the NADH-coupled assay. For all analyses, the time course of fluorescence decrease was measured using a Synergy NEO microplate reader ($\lambda_{ex} = 340$ nm, 440 nm emission filter). The rate from a control reaction with no ATP (background rate of fluorescence decrease) was subtracted from all rates. Katanin and FIGL1 were assayed at 50–75 nM. VPS4B was assayed at 100–200 nM. VCP/p97 was assayed at 300 nM. Analyses of chemical inhibitors were carried out in the same conditions using assay buffers supplemented with 0.1 mg ml^{-1} BSA and 0.005% vol/vol Triton X-100. Briefly, compounds dissolved in DMSO were added to the corresponding assay buffer, and a solution containing the ATPase and the NADH-coupled ATP regeneration system was added. The mixture was incubated for 5–30 min at room temperature under mild agitation before the addition of MgATP (1 mM final). The final DMSO concentration was 1%.

The assay buffers used were as follows:

Human katanin: 20 mM HEPES.Na, 120 mM NaCl, 5 mM $MgCl_2$, 1 mM TCEP, pH 7.4.

X. laevis katanin: 20 mM HEPES.Na, 120 mM NaCl, 5 $MgCl_2$, 5 mM $(NH_4)_2SO_4$, 1 mM TCEP, pH 7.4.

FIGL1: 20 mM HEPES.Na, 120 mM NaCl, 5 mM $MgCl_2$, 5 mM $(NH_4)_2SO_4$, 1 mM TCEP, pH 7.4.

VCP/p97: 20 mM HEPES.Na, 20 mM NaCl, 10 mM $MgCl_2$, 5 mM $(NH_4)_2SO_4$, 1 mM TCEP, pH 7.4.

HS-VPS4B: 25 mM HEPES.K, 25 mM KOAc, 2 mM $MgCl_2$, 5 mM $(NH_4)_2SO_4$, 1 mM TCEP, pH 7.4.

VPS4B: 20 mM HEPES.K, 25 mM KOAc, 2 mM $MgCl_2$, 5 mM $(NH_4)_2SO_4$, 0.5 mM $CaCl_2$, 1 mM TCEP, pH 7.4.

Equation used for data fitting. As the ATPase activity of AAA proteins exhibits a sigmoidal dependence on ATP concentration[13], in line with our previous work[14,17], we analyzed the enzyme activity using a modified Michaelis–Menten equation, which included a Hill coefficient[14]. In particular, to determine the enzyme activity parameters of AAA constructs we fitted rates from steady-state ATPase data to equation (1):

$$V = \text{ATPase rate} = (V_{max}x^h)/(K_{1/2}^h + x^h) \quad (1)$$

In this equation, V_{max} denotes the maximum ATPase rate, h is the Hill coefficient, x denotes ATP concentration and $K_{1/2}$ is the ATP concentration required for the half-maximal enzyme rate and has units of concentration (for example, mM). We adopted the $K_{1/2}$ annotation to distinguish this constant from the standard Michaelis constant, K_m. Catalytic turnover number (k_{cat}) was calculated by dividing the V_{max} value by the concentration of enzyme in the assay. For the compound IC_{50} calculation, for each experiment the measured enzyme activity was plotted against concentration of compound and the data were fit using a sigmoidal dose–response curve equation (2) to determine the IC_{50} value. The values from independent experiments were averaged and standard deviations, or ranges when appropriate, were calculated:

$$Y = \%\ \text{ATPase rate relative to DMSO control} = (Y_{min}) + ((Y_{max} - Y_{min})/(1 + 10^{(\log IC_{50} - x)h})) \quad (2)$$

Cell culture, generation of kata-WT and kata-D210C cell lines, and viability assays. HeLa TREx Flp-In cells were generated from HeLa TREx cells (Thermo Fisher cat. no. R71407) using the pFRT/*lac*Zeo vector (Thermo Fisher cat. no. V601520) according to the vendor's protocols. Kata-WT and kata-D210C cell lines were generated from the HeLa TREx Flp-In cells using pOG44 plasmid and the pcDNA5.0/FRT/TO vector containing EGFP-tagged full-length katanin-WT or -D210C (described in the 'Plasmids' section of the Methods). Genomic DNA was extracted from cells using the DNeasy Blood and Tissue kit (Qiagen); insertions were PCR-amplified and sequenced. Cells were cultured in DMEM (high glucose with sodium pyruvate and L-glutamine, Thermo Fisher) supplemented with 10% (vol/vol) FBS (Sigma-Aldrich) and hygromycin B (200 μg ml^{-1}) at 37 °C and 5% CO_2. Cells were confirmed to be mycoplasma-free using a PCR-based method[43].

For western blotting, cells were cultured with doxycycline (10 ng ml^{-1} for 24 h) before lysis at 4 °C. The following antibodies were used: rabbit monoclonal anti-p60 katanin (1:1,000; EPR5071; Abcam) and mouse monoclonal anti-GAPDH (1:1,000; 1E6D9; Proteintech). Membranes were imaged using a LI-COR Odyssey Infrared Imager. As done previously[13], cell viability assays were conducted using a CellTiter-Glo luminescent cell viability assay (Promega) according to the manufacturer's recommendations. The luminescence signal was quantified using a Synergy Neo microplate reader.

Live-cell imaging. Kata-WT and kata-D210C cells were grown on 22×22-mm coverslips in doxycycline (10 ng ml^{-1} for 18 h) and mounted in a custom Rose chamber in L-15 medium without phenol red (Invitrogen) supplemented with 10% FBS, and maintained at 37 °C. Confocal GFP fluorescence micrographs were acquired using a Nikon Eclipse Ti2-E microscope (Morrell Instruments), with a 100× objective (Plan Apo, 1.45 NA), a Yokogawa CSU10 confocal head and an EMCCD Prime 95B sCMOS camera (Photometrics). The laser was transmitted to the sample using a custom Yokogawa quad notch filter (405-480-561-640) and fluorescence from the EGFP was excited with a 100-mW, 488-nm (Coherent) laser.

Immunofluorescence. Cells were plated on acid-washed coverslips (#1.5; Fisher brand, cat. no. 12-545-81) coated with poly-D-lysine hydrobromide (Sigma, cat. no. P6407) and cultured for 48 h before fixation, with doxycycline (10 ng ml^{-1}) for 18 h pre-fixation and inhibitor (or 0.1% DMSO) treatment 4 h pre-fixation. Cells were fixed at −20 °C using methanol for 15 min. Coverslips were blocked (3% BSA and 0.1% Triton X-100 in phosphate-buffered saline) for 30–60 min. Cells were stained with rabbit polyclonal anti-CAMSAP2 antibody (Proteintech, cat. no. 17880-1-AP, 1:1,000 dilution) and mouse monoclonal anti-α-tubulin antibody (DM1A, Sigma, cat. no. T6199, 1:200 dilution) for microtubule staining experiments for 2.5 h, followed by Texas Red-conjugated anti-rabbit secondary antibody (Jackson Immunoresearch,1:500 dilution) (and Alexa 488-conjugated anti-mouse secondary antibody (Abcam, cat. no. 150113, 1:500 dilution) for microtubule staining experiments) for 60 min. DNA was stained with 4′,6-diamidino-2-phenylindole dilactate (Invitrogen cat. no. D3571, 0.5 μg ml^{-1}). Confocal fluorescence images were acquired as Z-stacks with 0.5-μm step size using a Nikon Eclipse Ti2-E microscope with a 100× objective (Plan Apo, 1.45 NA). For CAMSAP2 stretch length quantification, regions of interest (~9 μm×~9 μm) were selected for interphase cells with intact nuclei. EGFP-kata signal levels varied across cells, and cells with no detectable signal or those with clear aggregates were not analyzed (<5% total cells). CAMSAP2 stretch length measurements were made manually on maximum intensity projection images. For statistical comparison between the data from kata-WT and kata-D210C cells, DMSO-treated and ASPIR-1-treated, we used the Kruskal–Wallis test with a Dunn's multiple comparison correction in GraphPad Prism.

Crystallization, data collection and structural analysis. VPS4B-D135C (200 μM) was mixed with ASPIR-2 (500 μM) and initial crystallization screens with the MB Class Suite (Nextal Biotech) were performed using the hanging-drop vapor diffusion method at 18 °C. Subsequent crystallization screens were performed around the 100 mM K.HEPES pH 7.5, 10% PEG4000 and 100 mM $(NH_4)_2SO_4$ condition. The obtained crystals were flash-frozen in cryo-protected mother liquor containing 20% glycerol. X-ray diffraction data were collected at a wavelength of 0.92 Å and a temperature of 100 K with an Eiger2 9M detector at Brookhaven National Laboratory (beamline 17-ID-1, AMX). The diffraction data were processed using the fastdp program, based on XDS[44,45]. The structure was determined by molecular replacement in PHENIX[46] using PDB 1XWI[30] as a search model in Phaser[47]. The molecular replacement search model had all waters and ligands removed. Model building and refinement were performed using Coot and PHENIX[46,48]. The model was built with R_{work} and R_{free} values of 0.209 and 0.267, respectively, and Ramachandran statistics of 95.89% favored, 3.77% allowed and 0.34% outliers, and 0% rotamer outliers. Simulated annealing omit maps were generated using the model, deleting the inhibitor, and processing using PHENIX refine[49]. Simulated annealing omit map figures and $2F_o$-F_c density map figures were generated using contours of 3.0σ and 2.0σ, respectively, and atom radius (carve) = 2.0. The coordinates for the ASPIR-2 inhibitor were generated by using the SMILES string in eLBOW[50] to generate a CIF file. Table 1 statistics were generated using the PHENIX validation tool MolProbity[51]. The structure was deposited in the Protein Data Bank and assigned accession code 7L9X.

Reporting Summary. Further information on research design is available in the Nature Research Reporting Summary linked to this Article.

Data availability

The structure of VPS4B-D135C bound to ASPIR-2 has been deposited in the Protein Data Bank (PDB) under accession code PDB 7L9X. Data generated or analyzed during this study are included in this published Article (and its Supplementary Information files). Source data are provided with this paper.

References

43. Uphoff, C. C. & Drexler, H. G. Detection of mycoplasma contaminations. *Methods Mol. Biol.* **946**, 1–13 (2013).
44. Miller, M. S. et al. Getting the most out of your crystals: data collection at the new high-flux, Microfocus MX beamlines at NSLS-II. *Molecules* **24**, 496 (2019).
45. Kabsch, W. XDS. *Acta Crystallogr. D Biol. Crystallogr.* **66**, 125–132 (2010).
46. Adams, P. D. et al. PHENIX: a comprehensive Python-based system for macromolecular structure solution. *Acta Crystallogr. D Biol. Crystallogr.* **66**, 213–221 (2010).
47. McCoy, A. J. et al. Phaser crystallographic software. *J. Appl. Crystallogr.* **40**, 658–674 (2007).
48. Emsley, P., Lohkamp, B., Scott, W. G. & Cowtan, K. Features and development of Coot. *Acta Crystallogr. D Biol. Crystallogr.* **66**, 486–501 (2010).
49. Afonine, P. V. et al. Towards automated crystallographic structure refinement with phenix.refine. *Acta Crystallogr. D Biol. Crystallogr.* **68**, 352–367 (2012).
50. Moriarty, N. W., Grosse-Kunstleve, R. W. & Adams, P. D. Electronic Ligand Builder and Optimization Workbench (eLBOW): a tool for ligand coordinate and restraint generation. *Acta Crystallogr. D Biol. Crystallogr.* **65**, 1074–1080 (2009).
51. Chen, V. B. et al. MolProbity: all-atom structure validation for macromolecular crystallography. *Acta Crystallogr. D Biol. Crystallogr.* **66**, 12–21 (2010).

Acknowledgements

We thank J. Ross (UMass Amherst) for providing the *H. sapiens* katanin-p60 plasmid. T.M.K. is grateful to the NIH (GM130234) and Starr Cancer Consortium (I12-0055) for supporting this research. T.C. was supported in part by the 2018 Kestenbaum Award for Neurodegeneration. N.H.J. was supported in part by the National Science Foundation Graduate Research Fellowship Program (2017242069) and the NIH T32 GM115327 Chemistry-Biology Interface Training Grant to the Tri-Institutional PhD Program in Chemical Biology. M.J.G. was supported in part by an NCI T32 Training Grant (5 T32 CA 9673-40). We are grateful to the High Throughput and Spectroscopy Resource Center at The Rockefeller University for instrument use. We also thank Michael Oldham and Jue Chen (The Rockefeller University) and Deena Oren (Structural Biology Resource Center at The Rockefeller University) for equipment use and for engaging in helpful discussions regarding crystallography experiments. This research used the 17-ID-1 beamline of the National Synchrotron Light Source II, a US Department of Energy (DOE) Office of Science User Facility operated for the DOE Office of Science by Brookhaven National Laboratory under contract no. DE-SC0012704.

Author contributions

T.C., N.H.J. and T.M.K. conceived the project and designed experiments. T.C., N.H.J., M.J.G. and R.P. carried out protein biochemistry. T.C. and N.H.J. synthesized compounds. T.C. completed the computational docking analysis. T.C., N.H.J. and M.J.G. performed assays and analyzed data. N.H.J. engineered cell lines and acquired and analyzed cell imaging data. M.J.G. performed structural biology experiments. T.M.K. supervised the research. T.C., N.H.J. and T.M.K. wrote the manuscript with input from all authors.

Competing interests

The authors declare no competing interests.

Additional information

Extended data is available for this paper at https://doi.org/10.1038/s41594-021-00575-9.

Supplementary information The online version contains supplementary material available at https://doi.org/10.1038/s41594-021-00575-9.

Correspondence and requests for materials should be addressed to T.M.K.

Peer review information *Nature Structural & Molecular Biology* thanks Petra Wendler and the other, anonymous, reviewer(s) for their contribution to the peer review of this work. Peer reviewer reports are available. Inês Chen and Florian Ullrich were the primary editors on this article and managed its editorial process and peer review in collaboration with the rest of the editorial team.

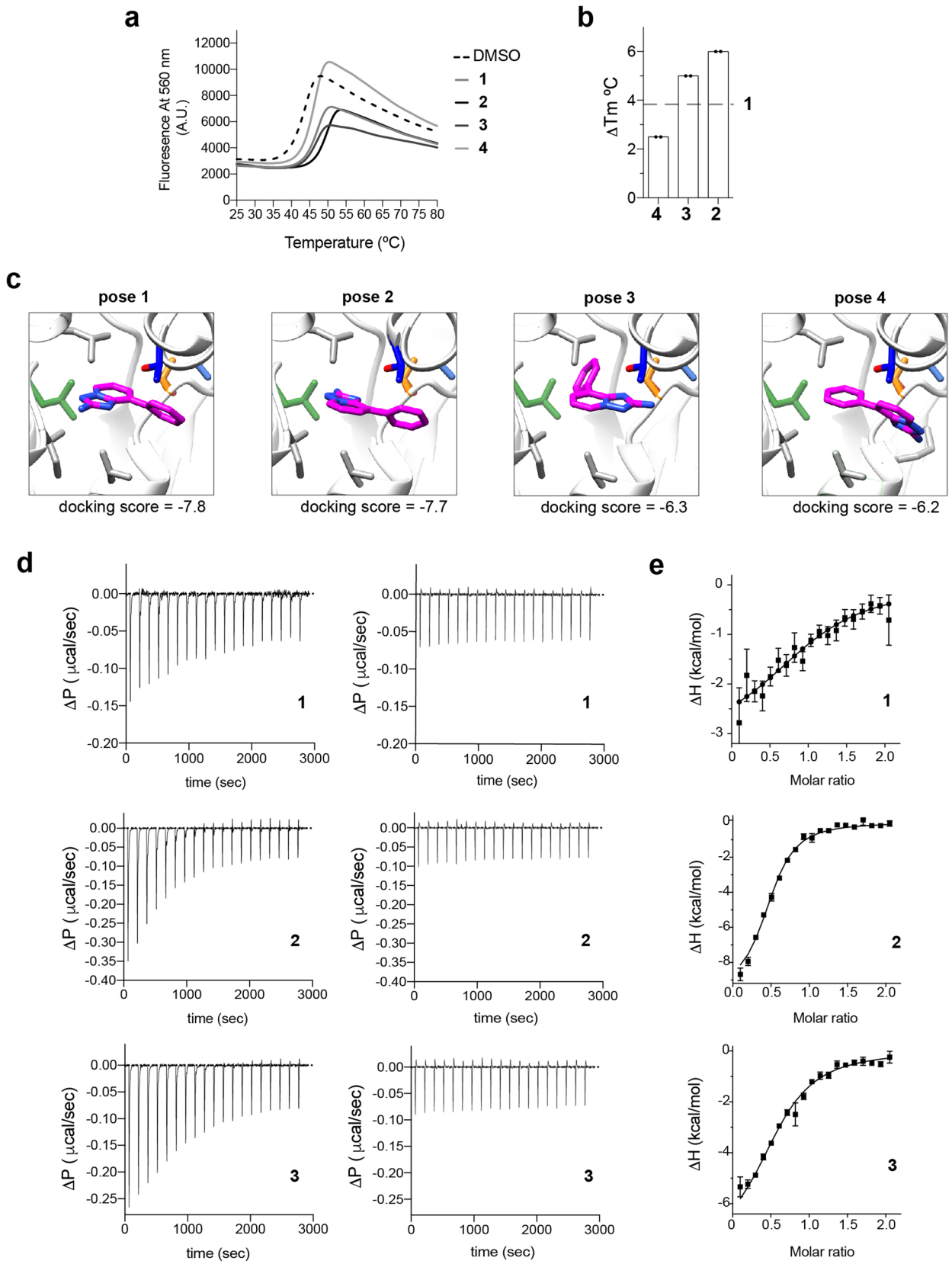

Extended Data Fig. 1 | See next page for caption.

Extended Data Fig. 1 | Characterizing the binding mode of triazolopyridine-based compounds to katanin. (**a-b**) DSF traces (**a**) and changes in melting temperatures (ΔTm, **b**) for kata-AAA-WT in the presence of compounds **1-4** (500 μM, n = 2). As a reference, the corresponding trace for control is shown (5% DMSO, dashed line, data in Fig. 1d). (**c**) Four computational docking models for compound **1** (purple and blue, stick representation) bound to the katanin nucleotide-binding site (gray, ribbon representation). Variability hotspot residues are shown (stick representation, color-coded as in Fig. 1a). Other key amino acids in the katanin ATP-binding site are also shown (gray, stick representation). Pose **1** corresponds to the one in Fig. 2e. (**d**) Isothermal Titration Calorimetry (ITC)-based analyses of kata-AAA-WT in the presence of compounds **1-3**. Raw injection heats are shown for titrations of compounds **1-3** against kata-AAA-WT (left panels), or compound titrations into buffer (right panels). Compound **4** could not be analyzed under similar conditions due to limited solubility. (**e**) Integrated data points and fitted binding curves used to determine K_d values. Data for graphs in (**a-b**) and (**d-e**) are available as source data.

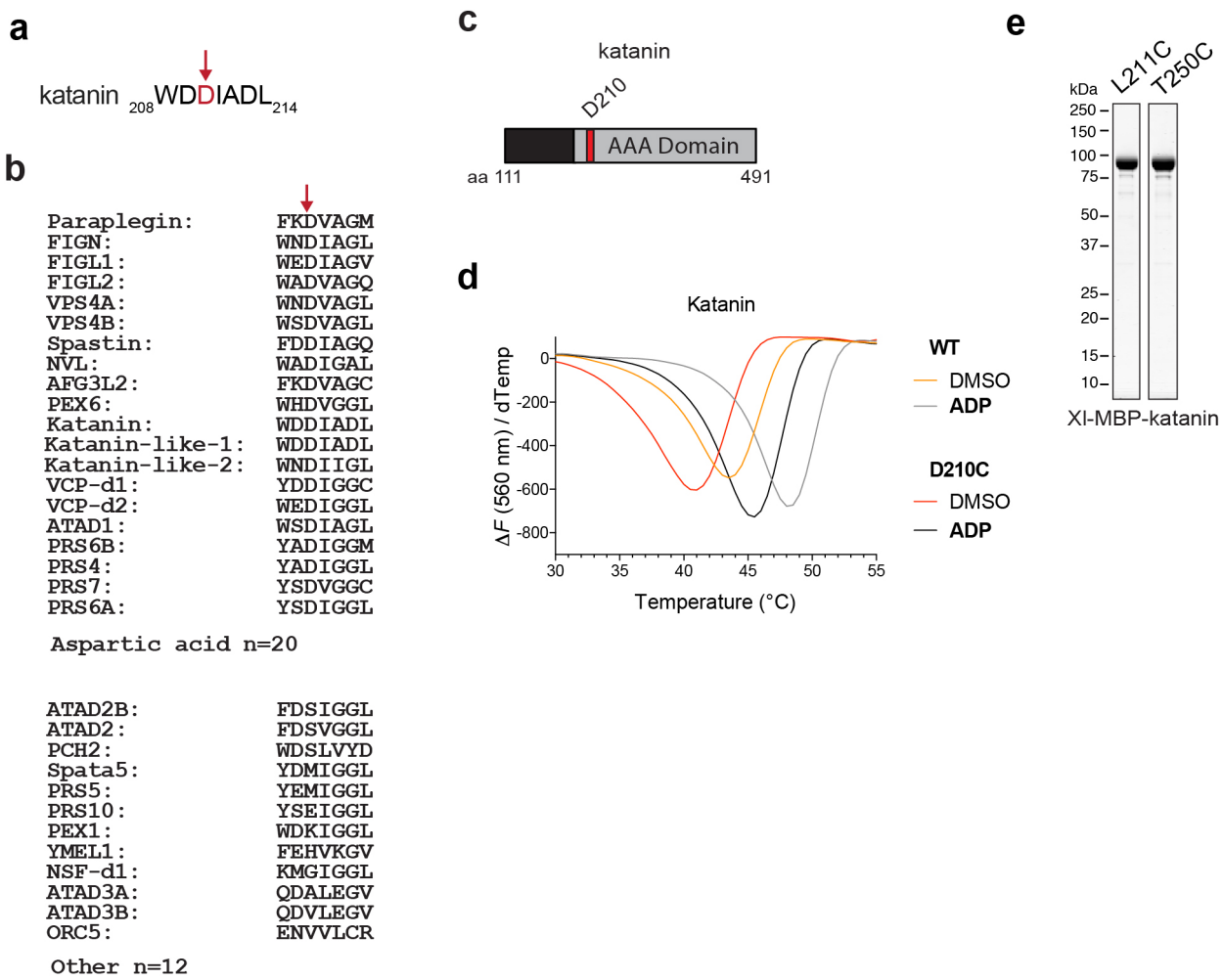

Extended Data Fig. 2 | Engineering the active site of katanin to obtain an allele sensitized to covalent inhibitors. a, Primary sequence of the katanin N-loop motif, which contains D210. **b**, Partial sequence alignment of AAA proteins showing the residues in the N-loop motif (D210 is indicated by the arrow, alignment generated using Clustal Omega). **c**, Schematic showing the AAA domain (light gray box, not to scale), and the first and last residues of the ATPase active human katanin construct. The position of the D210C mutation is indicated by the red bar. **d**, Differential scanning fluorimetry of katanin-WT and katanin-D210C in the absence and presence of ADP (1 mM) (n = 2 independent experiments). One representative experiment is shown. **e**, SDS-PAGE gels of purified recombinant L211C and T250C *X. laevis* katanin mutant constructs (Coomassie blue staining). Data for the graph in (**d**) and the unmodified gel picture for (**e**) are available as source data.

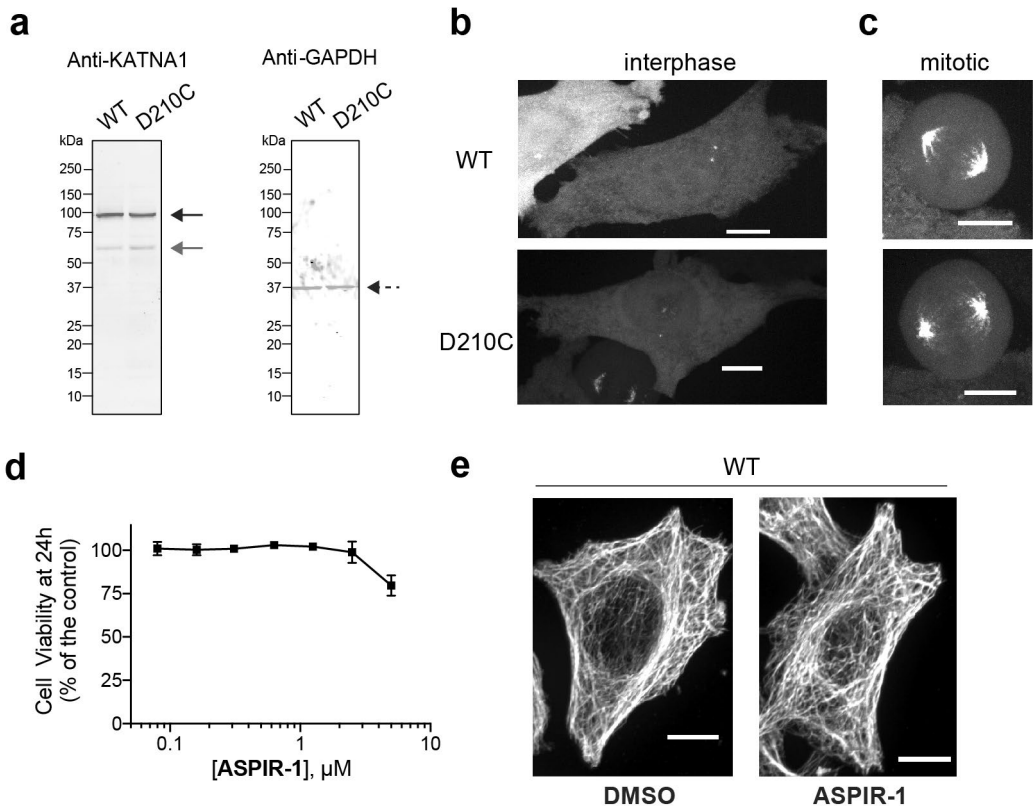

Extended Data Fig. 3 | Characterization of kata-WT and kata-D210C cell lines and additional analyses of ASPIR-1. a, Full blots for Fig. 4a. Doxycycline (10 ng/mL, 14 hours) was used to induce expression and blot was stained for katanin (left panel) and GAPDH (right panel) as a loading control. The positions of the bands expected for the EGFP-katanin construct and the endogenous katanin (black and gray arrows, respectively), or GAPDH (black dotted arrow) are indicated. A representative blot is shown (n = 2 independent cell cultures per cell line). (**b-c**) Maximum intensity confocal projections show EGFP distribution in interphase (**b**) and dividing (**c**) HeLa cells expressing WT or D210C EGFP-katanin. Representative images are shown (n = 2 independent experiments, 10 images acquired per experiment). **d**, Kata-WT cells were incubated with different concentrations of ASPIR-1 for 24 h and viability was measured using a CellTiter-Glo Luminescent Cell Viability Assay. Data are mean ± s.d., n = 3 independent experiments. **e**, Microtubule organization in fixed kata-WT cells treated for 4 hours with ASPIR-1 (1.25 μM) or control (DMSO, 0.1%) and stained for α-tubulin. Representative images, identically contrasted maximum intensity projections are shown (n = 3 independent experiments, 10 images acquired per condition per experiment, scale bar =10 μm). The uncropped blots for (**a**) and data for the graph in (**d**) are available as source data.

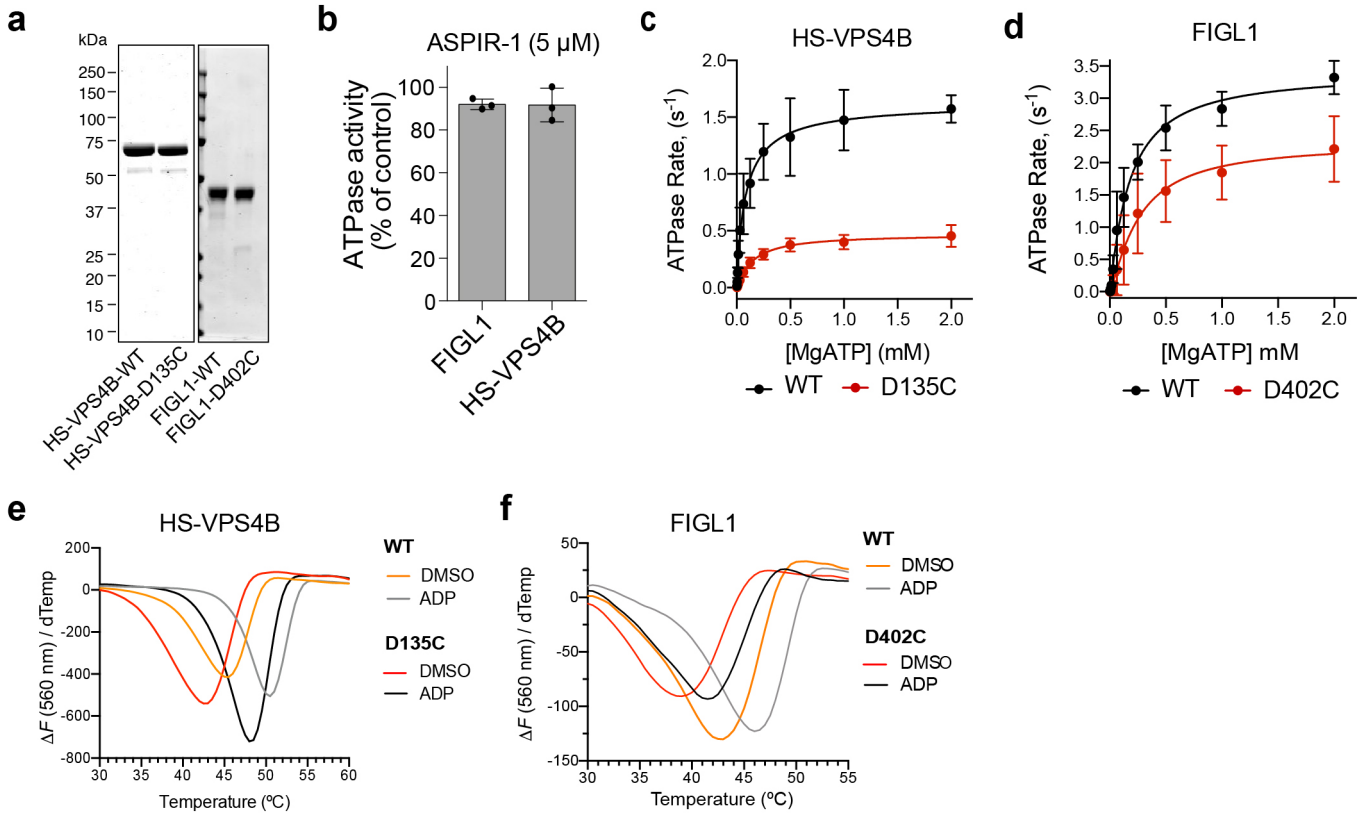

Extended Data Fig. 4 | Effect of the inhibitor-sensitizing Asp-to-Cys mutation on the AAA proteins VPS4B and FIGL1. a, SDS–PAGE analysis of purified recombinant human wild type (WT) and mutant (D135C) HS-VPS4B constructs, and wild type and mutant (D402C) FIGL1 constructs (Coomassie blue staining). **b**, Percentage steady-state ATPase activity of FIGL1 and HS-VPS4B (WT) in the presence of ASPIR-1 (5 μM, 1 mM ATP, 30 min incubation; data represent mean ± s.d., n = 3 independent experiments). (**c-d**) ATP concentration dependence of the steady-state activity of WT and D135C HS-VPS4B (**c**), and WT and D402C FIGL1 (**d**) analyzed using an NADH-coupled assay. Rates were fit to the Michaelis–Menten equation for cooperative enzymes (mean ± range, n = 2 independent experiments for HS-VPS4B-WT and HS-VPS4B-D135C; mean ± s.d., n = 5 independent experiments for FIGL1-WT, n = 7 independent experiments for FIGL1-D402C). Kinetic parameters were determined: k_{cat} = 1.7 ± 0.1 s^{-1}, $K_{1/2}$ = 0.12 ± 0.07 mM for HS-VPS4B-WT; k_{cat} = 0.5 ± 0.1 s^{-1}, $K_{1/2}$ = 0.15 ± 0.01 mM for HS-VPS4B-D135C; k_{cat} = 3.4 ± 0.4 s^{-1}, $K_{1/2}$ = 0.2 ± 0.1 mM for FIGL1-WT; k_{cat} = 2.3 ± 0.5 s^{-1}, $K_{1/2}$ = 0.3 ± 0.1 mM for FIGL1-D402C. (**e-f**) Differential scanning fluorimetry of WT and D135C HS-VPS4B (**e**) and WT and D402C FIGL1 (**f**) in the absence and presence of ADP (1 mM) (5% DMSO for both conditions). One representative experiment is shown (n = 2 independent experiments). The unmodified gel images for (**a**) and data for the graphs in (**b-f**) are available as source data.

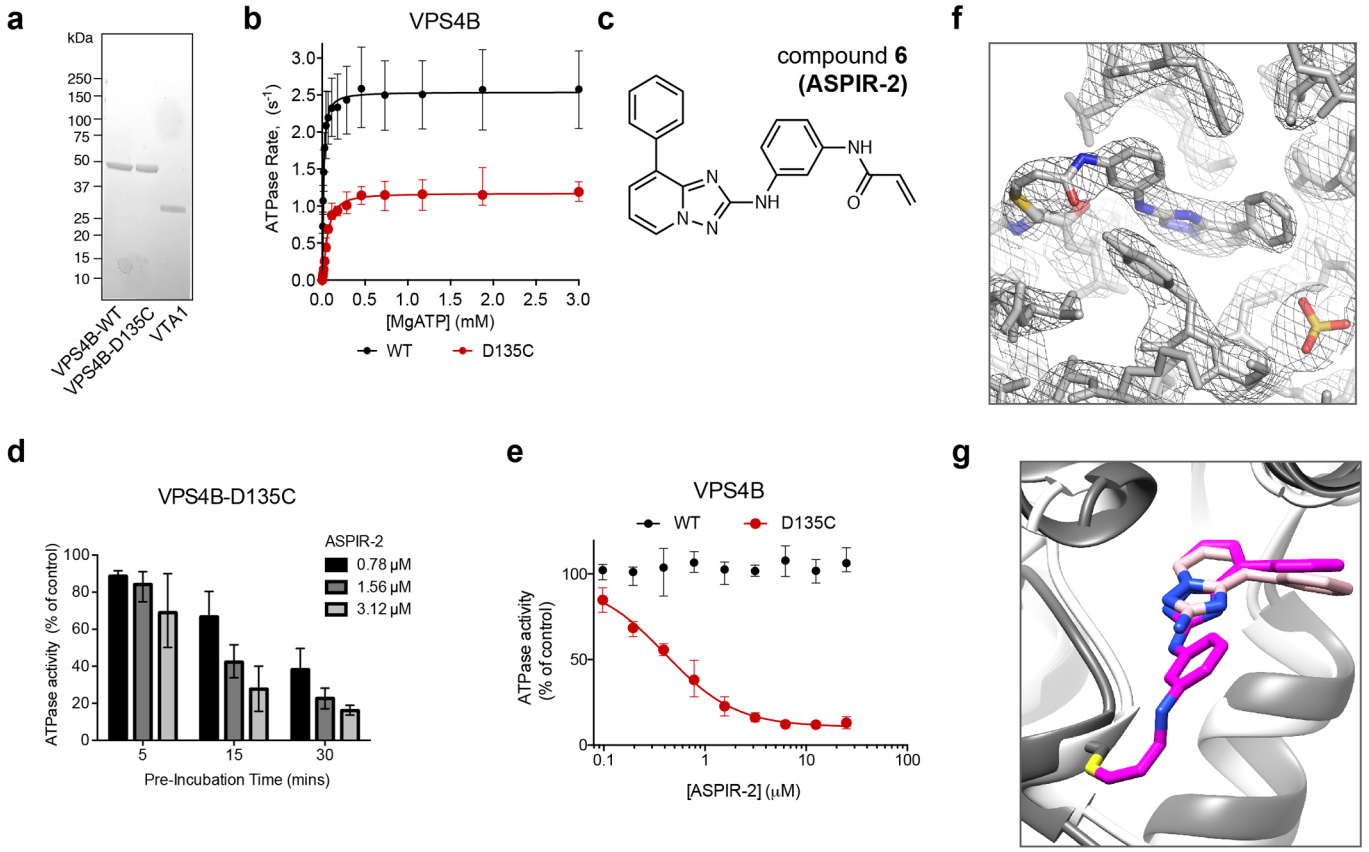

Extended Data Fig. 5 | Inhibition of VPS4B-D135C by ASPIR-2. a, SDS–PAGE analysis of purified recombinant human wild type (WT) and mutant (D135C) VPS4B (tagless), and VTA1 constructs (Coomassie blue staining). **b**, ATP-concentration dependence of the steady-state activity of VPS4B-WT and VPS4B-D135C in the presence of 2-fold excess VTA1, analyzed using an NADH-coupled assay. Rates were fit to the Michaelis–Menten equation for cooperative enzymes (mean±range, n = 2 independent experiments). **c**, Chemical structure of ASPIR-2, the analog used for x-ray crystallography studies. **d**, Time-dependent inhibition of the ATPase activity of VPS4B-D135C by ASPIR-2. Graph shows percentage residual ATPase activity (mean ± range, n = 2 independent experiments). **e**, Concentration-dependent inhibition of the VTA1-stimulated, steady-state ATPase activity of WT and D135C VPS4B after 30 min incubation with ASPIR-2 (1 mM ATP; data represent mean ± range, n = 2 independent experiments). **f**, $2F_o$-F_c electron density map of the crystal structure of VPS4B-D135C bound to ASPIR-2, contoured at 2.0 σ. **g**, Overlay of the structure of VPS4B-D135C in complex with ASPIR-2 with the RADD model for compound **1** bound to katanin, at the nucleotide-binding site (ASPIR-2: purple and blue, compound **1**: pink and blue, stick representation; VPS4B-D135C: gray, katanin: white, ribbon representation; VPS4B residue Cys-135 is also shown). The unmodified gel image for (**a**) and data for the graphs in (**b**) and (**d-e**) are available as source data.

nature research

Corresponding author(s): Tarun Kapoor

Last updated by author(s): Feb 1, 2021

Reporting Summary

Nature Research wishes to improve the reproducibility of the work that we publish. This form provides structure for consistency and transparency in reporting. For further information on Nature Research policies, see our Editorial Policies and the Editorial Policy Checklist.

Statistics

For all statistical analyses, confirm that the following items are present in the figure legend, table legend, main text, or Methods section.

n/a	Confirmed
☐	☒ The exact sample size (*n*) for each experimental group/condition, given as a discrete number and unit of measurement
☐	☒ A statement on whether measurements were taken from distinct samples or whether the same sample was measured repeatedly
☐	☒ The statistical test(s) used AND whether they are one- or two-sided *Only common tests should be described solely by name; describe more complex techniques in the Methods section.*
☐	☒ A description of all covariates tested
☐	☒ A description of any assumptions or corrections, such as tests of normality and adjustment for multiple comparisons
☐	☒ A full description of the statistical parameters including central tendency (e.g. means) or other basic estimates (e.g. regression coefficient) AND variation (e.g. standard deviation) or associated estimates of uncertainty (e.g. confidence intervals)
☐	☒ For null hypothesis testing, the test statistic (e.g. *F*, *t*, *r*) with confidence intervals, effect sizes, degrees of freedom and *P* value noted *Give P values as exact values whenever suitable.*
☒	☐ For Bayesian analysis, information on the choice of priors and Markov chain Monte Carlo settings
☒	☐ For hierarchical and complex designs, identification of the appropriate level for tests and full reporting of outcomes
☒	☐ Estimates of effect sizes (e.g. Cohen's *d*, Pearson's *r*), indicating how they were calculated

Our web collection on statistics for biologists contains articles on many of the points above.

Software and code

Policy information about availability of computer code

Data collection	Gel and western blot images were collected using Odyssey Application softare. Differential scanning fluorimetry data were collected using CFX Maestro software. Isothermal titration calorimetry data were collected using MicroCal iTC200 software. Simulations and compound docking were performed using the Schrodinger Meastro program package (version 12.2.02). ATPase and cytotoxicity data were collected using Gen5 software (verson 2.04) for BioTek Synergy NEO. Imaging data were collected uisng NIS-Elements AR software. Crystallographic data collection was carried out using Life Science Data Collection. For compounds, mass spectra were collected using MassLynx (version 4.2) software and nuclear magnetic resonance spectra were collected using TopSpin 2.1.
Data analysis	Sequence alignments were performed using Clustal Omega. Isothermal Titration Calorimetry data were analyzed in the AFFINImeter software. Western blots and immunofluorescence data were quantified using Fiji (ImageJ, version 2.0.0-rc-68/1.52g). Graphs for quantified data were plotted in GraphPad Prism (version 6). GraphPad Prism (version 6) was also used to fit ATP titration and inhibition curves for ATPase assays, and to determine statistical significance for immunofluorescence data (Kruskal-Wallis test with Dunn's multiple comparison correction). Crystallographic data processing was carried out using the fastdp program, PHENIX, Phaser, and Coot.

For manuscripts utilizing custom algorithms or software that are central to the research but not yet described in published literature, software must be made available to editors and reviewers. We strongly encourage code deposition in a community repository (e.g. GitHub). See the Nature Research guidelines for submitting code & software for further information.

Data

Policy information about availability of data

All manuscripts must include a data availability statement. This statement should provide the following information, where applicable:

- Accession codes, unique identifiers, or web links for publicly available datasets
- A list of figures that have associated raw data
- A description of any restrictions on data availability

The structure of VPS4B-D135C bound to ASPIR-2 has been deposited in the Protein Data Bank (PDB) under accession code 7L9X. Source data for graphs are available with the paper online. All other data generated or analyzed during this study are included in this published article (and its Supplementary Information files) or are available from the corresponding author on reasonable request. A Life Sciences Reporting Summary for this paper is available.

Field-specific reporting

Please select the one below that is the best fit for your research. If you are not sure, read the appropriate sections before making your selection.

☒ Life sciences ☐ Behavioural & social sciences ☐ Ecological, evolutionary & environmental sciences

For a reference copy of the document with all sections, see nature.com/documents/nr-reporting-summary-flat.pdf

Life sciences study design

All studies must disclose on these points even when the disclosure is negative.

Sample size	Preselection of sample size was not performed.
Data exclusions	No data were excluded from the analysis.
Replication	Attempts at replication of data were successful and statistics are reported as needed.
Randomization	All combinations were tested to control for covariates.
Blinding	Investigators were not blinded to group allocation in data analysis.

Reporting for specific materials, systems and methods

We require information from authors about some types of materials, experimental systems and methods used in many studies. Here, indicate whether each material, system or method listed is relevant to your study. If you are not sure if a list item applies to your research, read the appropriate section before selecting a response.

Materials & experimental systems

n/a	Involved in the study
☐	☒ Antibodies
☐	☒ Eukaryotic cell lines
☒	☐ Palaeontology and archaeology
☒	☐ Animals and other organisms
☒	☐ Human research participants
☒	☐ Clinical data
☒	☐ Dual use research of concern

Methods

n/a	Involved in the study
☒	☐ ChIP-seq
☒	☐ Flow cytometry
☒	☐ MRI-based neuroimaging

Antibodies

Antibodies used	Rabbit monoclonal anti-p60 katanin (EPR5071; Abcam), Mouse monoclonal anti-GAPDH (1E6D9; Proteintech), Rabbit polyclonal anti-CAMSAP2 (17880-1-AP; Proteintech), Mouse monoclonal anti-alpha-tubulin DM1A (T6199, Sigma)
Validation	All antibodies used have been previously cited.

Eukaryotic cell lines

Policy information about cell lines

Cell line source(s)	Cell lines were engineered in-house from commercial HeLa TREx cells.

Authentication	To confirm correct incorporation of KATNA1 (WT and D210C mutant), genomic DNA was extracted from cells using the DNeasy Blood and Tissue kit (Qiagen); insertions were PCR amplified and sequenced.
Mycoplasma contamination	Cells were confirmed to be mycoplasma free using a PCR-based method.
Commonly misidentified lines (See ICLAC register)	*Name any commonly misidentified cell lines used in the study and provide a rationale for their use.*